Turbulence Modulation of Polydisperse Particles in a Square Particle-Laden Jet: Numerical Investigation

Sandria Lutrica Gray

Thesis submitted to the faculty of the Virginia Polytechnic Institute and State University in partial fulfillment of the requirements for the degree of

Master of Science
In
Mechanical Engineering

Kenneth S. Ball, Co-Chair
Mary E. Kasarda, Co-Chair
Francine Battaglia

May 1, 2012

Blacksburg, Virginia

Keywords: polydispersion, turbulent intensity, square particle-laden jet

Turbulence Modulation of Polydisperse Particles in a Square Particle-Laden Jet: Numerical Investigation

Sandria L. Gray

Abstract

The purpose of this study is to numerically investigate the turbulence modulation of polydisperse particles in a square particle-laden jet. Turbulence modulation describes the effects of fluctuating velocity and intensity when the particles and continuous fluid interact in a turbulent flow field. The rate at which turbulence modulation is altered is dependent upon parameters such as particle size, mass loading, Stokes number, coupling, volume fraction and mechanisms of turbulence modulation. This study modifies the analytical model developed by Yarin and Hetsroni (1993) to account for the transitional drag regime for coarse polydisperse particles. The particles under study are dilute, inert and spherical, with relatively high Stokes numbers, and classified as having two-way coupling with the fluid. The new analytical model is compared to numerical results using the Computational Fluid Dynamics (CFD) software FLUENT (ANSYS, Inc.). The turbulence model employed is the standard k-ε model. This study will analyze the effects of varying mass content and particle ratios to investigate how turbulence modulation is influenced. The new model and the CFD results show good agreement in the cases where the mass contents of each particle size are equal. This study will also look into the effects of polydispersion, and the concentration distribution, for indoor air applications. It was found that, in certain cases, the monodisperse assumption slightly over-predicts the concentration distribution in the enclosed region.

Acknowledgements

Stand on the shoulders of Giants.

This quote is prominently displayed under the search box on the Google Scholar site. Every time I read it, it resonates differently within me. The reason being, I have been blessed to encounter many "Giants", be it family, friends, colleagues, faculty and staff, throughout my academic career.

Firstly, I would like to thank my advisors Dr. Kenneth Ball and Dr. Mary Kasarda. Both of you have played integral roles in my academic career, having challenged me to become more critical and independent in my research. Dr. Kasarda, I want to especially thank you for your constant words of encouragement and motivation. There were many times during which I became discouraged, but you were on-hand to provide me with inspiration. The GTA opportunities you provided have also been invaluable experiences. Dr. Ball, I want to especially thank you for giving me the freedom to be creative with my research project, which contributed greatly to me discovering my identity as a Graduate Student. This experience has proven to be invaluable in so many ways and I will always be grateful for it. Again, I thank you both.

To my professor and committee member Dr. Francine Battaglia, thank you for the knowledge and assistance that you have provided during my graduate career. I am very grateful.

A special thanks to Dr. Qingyan Chen from Purdue University for granting me permission to use the numerical code to obtain the concentration distribution for Lagrangian Particle Tracking.

I would also like to thank the TPANS research group for the help they provided towards my research. This group has been very helpful throughout this project. A special thanks to Christopher Sebesta and Debamoy Sen for their assistance with FLUENT (ANSYS, Inc.). I would also like to acknowledge the Mechanical Engineering Department, and the Graduate community as a whole. Many of the staff and students had been very eager to assist me with my research and adjusting to Graduate School.

I would not be where I am today without the strength and prayers of my family, and words of encouragement from my friends. Special thanks to my mother, Helen, and my sister, Candria, for the words of encouragement and continual prayer. I love you both. A huge thank you goes to the love of my life and future husband, Atiba. This would have been extremely difficult without you, especially considering the fact that you proofread this thesis several times! Thank you for consistently being loving and supportive. You are my rock!

Last but certainly not least, well actually unquantifiable, is God. I am extremely thankful for all of the "Giants" that you have placed on my path. This would also have not been possible without your guidance, presence, and many blessings.

For with God nothing shall be impossible.
Luke 1:37 (King James Version)

Table of Contents

List of Figures

List of Tables

Nomenclature

A	cross-sectional area [m^2]
a_1	constant in drag coefficient Eq. 4.10 [-]
a_2	constant in drag coefficient Eq. 4.10 [-]
a_3	constant in drag coefficient Eq. 4.10 [-]
$a(t)$	random acceleration term [m²/s]
C_1	term for omega multiplier [m/s]
C_2	term for omega multiplier [m/s]
C_μ	constants from standard k-ε model
$C_{1\varepsilon}$	constants from standard k-ε model
$C_{2\varepsilon}$	constants from standard k-ε model
$C_{3\varepsilon}$	constants from standard k-ε model
C	correction function for non-Stokesian flows [-]
C_c	Cunningham correction factor [-]
C_D	drag coefficient [-]
D	Diffusion coefficient [m²/s]
d	diameter or length [m]
F	force [N]
f	ratio of particle drag to Stokes drag [-]
f_{D1}	Doppler shift for a beam [Hz]
f_{D2}	Doppler shift for a beam [Hz]
g	gravity [m²/s]
G_k	turbulent kinetic energy from mean velocity gradient [m^2/s^2]
G_b	turbulent kinetic energy from buoyancy [m^2/s^2]
Δx	grid spacing [m]
l_e	turbulent length scale [m]
$\bar{l}$	dimensionless mixing length [-]

J	flux of particles [mol/m^2-s]
J_{Re}	drag-Reynolds coefficient
k	turbulent kinetic energy [$\frac{m^2}{s^2}$]
k_B	Boltzmann constant [$m^2 kg/s^2 K$]
K_0	coagulation coefficient [-]
K	corrected coagulation coefficient [-]
L_h	hybrid length scale [m]
L_i	interparticle spacing [m]
m	mass [kg]
m_c	ratio of mass content [-]
m^*	local loading [kg]
$\dot{m}$	mass flow rate [kg/s]
N	number of particles [-]
$\dot{q}$	volumetric flow rate of particles [m^3/s]
Re	Reynolds number [-]
S_k	user defined terms from standard k-ε model
S_ϵ	user defined terms from standard k-ε model
Stk	Stokes number [-]
T	absolute temperature [K]
T_f	characteristic time of the fluid in average motion [s]
T_L	large scale fluctuation of continuous phase [s]
t^*	particle interaction time [s]
TM	turbulence modulation parameter [-]
$\ddot{v}_i$	mean fluctuating velocity component [kg/s]
u^*	frictional velocity [m/s]
U_m	mean velocity [m/s]
V	velocity [m/s]
$\bar{V}$	mean velocity [m/s]

$\bar{V}'$ mean flucutating velocity [m/s]

$\dot{V}$ volume [m^3]

v' fluctuational velocity [m/s]

y^+ log law wall function [-]

y distance closest to the wall [m]

Y_m fluctuating dilation

GREEK LETTERS

β correction factor for coagulation [-]

γ mass content of particles [-]

ε rate of energy dissipation [m^2/s^3]

λ mean free path of gas

λ_w wavelength [m]

ρ density [kg/m^3]

θ angle of intersection between both beams [degrees]

τ_i particle response or relaxation time [s]

$\nabla.\tau_s$ tensor term [N]

τ time scale [s]

$\bar{\tau}^*$ dimensionless interaction time [-]

τ^* characteristic time [s]

$\Phi_{1,2}$ term used in eqn. 3.11 [-]

ϕ_p volume fraction of particles [-]

μ dynamic viscosity [$\frac{kg}{m-s}$]

ν kinematic viscosity [$\frac{m^2}{s}$]

ω particle diameter ratio [-]

ω^* omega multiplier [-]

Ω mass loading [-]

σ	turbulent Prandtl number [-]
ΔE_t	average kinetic energy modification [J]

SUBSCRIPTS

0	initial
avg	average
crit	critical
ε	rate of energy dissipation
ed	eddy
d	bulk for particle
D	drag
f	fluid
fr	fringe spacing
g	gas
G	bulk for gas
i	particle number index
in	inherent
k	kinetic energy
ko	Kolmogorov
L	large scale
m	mean
other	other
p	particle
rel	relative
s	settling velocity
sc	scattering particle
t	turbulent

Chapter 1: Introduction

1.1 MOTIVATION

In recent years there has been growing concern regarding biological terrorism, i.e., airborne contaminants such as anthrax being released in confined spaces and endangering the lives of innocent individuals. There has also been some concern expressed about the possibility of contaminants trapped in the ventilation ducts of public buildings eventually affecting indoor air quality, leading to chronic health effects. Arguably, the most important global concerns are the detrimental effects of fossil fuel combustion on our planet. Each of these concerns present different scenarios, yet they possess one commonly recurring theme – particle dispersion.

Research in particle dispersion is growing in importance as it is applied to situations that affect the world in which we inhabit. According to a report released by the World Health Organization (WHO), if 50 kg of a biological agent such as anthrax were dropped in an urban city, it would spread as far as 20 square kilometers, killing tens of thousands of people [1]. This statement alone supports the relevance of research in particulate transport. Researchers at Lawrence Berkeley National Labs are developing expressions to evaluate the risk assessment involved in the inhalation transfer factors (ITF) of particles that are dispersed in a room and outdoors [2]. With these expressions, they found that indoor emissions for ITF's were much higher than outdoors [2].

Engineering controls and prevention strategies are not only being implemented for particulate dispersion in biological terrorism, but also in health care facilities [3]. Because humans spend a significant amount of time indoors, it is vital that indoor air quality does not contribute to health issues. The Environmental Protection Agency (EPA) identifies some of the

building-related illnesses associated with poor indoor air quality as: Legionnaire's disease, asthma, hypersensitivity pneumonitis, and humidifier fever [4].

In addition to biological and health hazards of particulate matter, fossil fuels are becoming prevalent in the industrial world. Responsible for 85% of the anthropogenic carbon emissions released in the environment annually, fossil fuels are one of the major contributors to global warming [5]. The Intergovernmental Panel on Climate Change (IPCC) released a report predicting that the temperature of the earth will rise between 2 °F and 5.2 °F by the year 2099 [5]. During the last century, there was only an increase of 1.2 °F [6]. Scientists and engineers are researching ways in which emissions and pollution can be reduced. Although the efficiency of diesel is higher than that of natural gas, it emits more pollution, i.e., nitrous oxides and particulate matter into the environment [7]. The pollution and particulate matter can pose as a health risk and contribute to global warming. Scientists at Argonne National Laboratory are developing ways to improve the efficiency of diesel and gas engine sprays to reduce the amount of emissions into the environment [7]. The scientists developed an absorption technique that is non-intrusive and produces a high characterization of mass distribution in diesel and gas engine sprays [7]. In order to contribute to the existing knowledge and current understanding of biological agents such as anthrax, particles that are trapped in ventilation systems, and global warming from diesel engine sprays, numerical models must be employed. For validation purposes, experiments must also be conducted.

The examples above outline the importance of research in particle dispersion. In turbulent flows, particle dispersion can greatly impact the turbulence modulation in a flow-field. Turbulence modulation is the process in which the turbulence intensity and the fluctuating velocity of the continuous fluid change due to the onset of particles in the flow-field. Previous

studies have shown that turbulence modulation can have strong effects on flows with a small number of particles [8]. The goal of this current research is to provide more understanding in turbulence modulation using numerical methods. The aim is to provide further knowledge and understanding of the gas-solid systems and to provide insight on the dispersion of anthrax. This, in turn could lead to reducing or completely eliminating particles from HVAC equipment, and improving the efficiency of diesel and gas engine sprays and many multiphase systems alike.

Understanding the characteristics of particle dispersion is crucial to accurately predicting these types of multiphase flows. Experimental models are typically created on a small scale, due to the expense of building large-scale models. One of the advantages of using Computational Fluid Dynamics (CFD) is that it is cost-effective. CFD models will never replace experiments and theory, but they can accompany them and are useful in validating each other. CFD is becoming more popular and widely accepted in characterizing the phenomena of particle dispersion. This is due mainly to the availability of commercial codes such as FLUENT (ANSYS, Inc.) that allow engineers and scientists to evaluate the characteristics of dispersion properties such as velocity, pressure, and concentration.

1.2 Project Overview and Thesis Objectives

The aim of this thesis is to increase the knowledge and further the understanding of turbulence modulation in particle-laden jets. To accomplish this, numerical simulations are modeled in FLUENT (ANSYS, INC.) and validated by the modification of an analytical model developed by Yarin and Hetsroni [9] that accounts for particles in the transitional drag regime. Previous studies have shown that turbulence modulation have effects flows with both large and small particles [10]. This study will explore how coarse particles of different sizes and densities

affect the modulation in a dilute flow-field. Figure 1 displays the geometry and dimensions of the particle-laden jet that is under study. As shown in the figure, there is one inlet and outlet, on opposite faces. Particles of two different sizes will be injected into the room at a certain velocity and turbulence intensity with a constant mass flow rate. The inlet and outlet are centered about the z-axis. This geometry was selected because it models a small room that has been scaled down to model computationally.

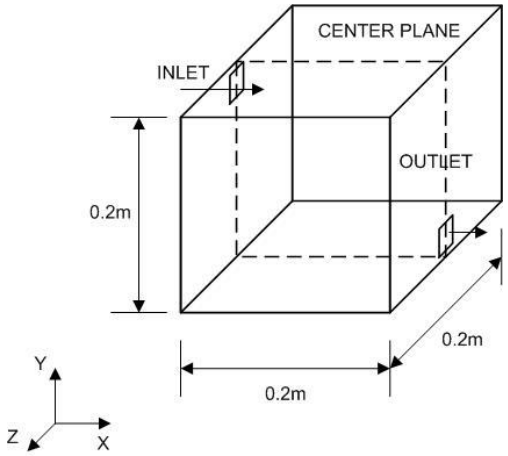

Figure 1-1: Schematic of Model Geometry with Dimensions

This thesis has three main objectives:

1. Use CFD to predict turbulence modulation on spherical bidisperse particles (size and density variation) surrounded by air in a square particle laden jet in dilute phase.
2. Develop and modify an existing analytical model for turbulence intensity and polydispersion to account for particles in the transitional drag regime.
3. Study the effects of how concentration changes with monodisperse and bidisperse spherical particles in enclosed regions, and ascertain whether the difference is significant.

1.3 SCOPE OF WORK

Chapter 2 is a review of the background and literature in relation to turbulence modulation in particle-laden jets. Chapter 3 will summarize the work done by Yarin and Hetsroni [9] and outline the major assumptions of their work. Chapter 4 will explain the equations of motion and explain the parameters used in FLUENT (ANSYS, INC.) and will conclude with a grid independence study. Chapter 5 will discuss and compare the results obtained from the new proposed analytical model and compare it with the CFD results for the square particle-laden jet. Chapter 6 will summarize the results and discuss future work to further this research.

Chapter 2: Background and Review of Literature

2.1 Introduction

This chapter will begin by discussing important concepts used in turbulent modulation as well as some of the work done in previous research. Next, some of the major work done with particle-laden jets, and some of the trends observed experimentally, analytically, and numerically will be highlighted. Lastly, some of the ways in which turbulence modulation is measured in experiments and the advantages/disadvantages associated with certain methods will be discussed. This research will only be concerned with dilute flows. A flow is considered dilute when the volume fraction of the particles is lower than 10^{-3} [11].

2.2 Important Concepts in Turbulence Modulation

Turbulence modulation occurs when particles alter the turbulent structure of the continuous phase. The intensity of the alteration determines how much the turbulent flow has modulated. There are many important concepts that must be understood with this phenomenon. Properties such as Stokes number, mass loading ratio, particle size, coupling, volume fraction and the mechanisms of turbulent modulation all play a major role in turbulence modulation and can have significant impact on the phenomenon.

2.2.1 Stokes Number

The Stokes number is an important parameter in heterogeneous turbulent flows. This dimensionless parameter depicts how a particle will respond to fluctuations in turbulent flow. Because the nature of turbulence has both length and time scales, the Stokes number is defined as:

$$Stk_f = \frac{\tau_p}{T_f} \tag{2.1}$$

where Stk_f is the Stokes number in averaged motion, τ_p is the particle response time, and T_f is the characteristic time of the fluid in average motion [12]. The particle response time indicates the time it takes for the particle to respond to the continuous phase and it can be described as:

$$\tau_p = \frac{\rho_p d_p^2}{18\mu C} \tag{2.2}$$

where C is the correction function for non-Stokesian flows [12]. For Stokesian flows, C = 1. For non-Stokesian flows, the correction function can be calculated using the expression below, based on the particle Reynolds number as:

$$C = 1 + \frac{Re_p^{\frac{2}{3}}}{6} \; at \; Re_p \leq 10^3 \tag{2.3}$$

$$C = \frac{0.11 Re_p}{6} at \; Re_p > 10^3 \tag{2.4}$$

where the particle Reynolds number, Re_p, is the relative velocity between the continuous and discrete phase

$$Re_p = \frac{|\vec{v} - \vec{v}_p| d_p}{\upsilon} \tag{2.5}$$

For large-scale fluctuation, the Stokes number can be defined as:

$$Stk_L = \frac{\tau_p}{T_L} \tag{2.6}$$

where T_L is the large-scale fluctuation of the continuous phase [12]. For small-scale fluctuation, the Stokes number can be defined as:

$$Stk_{Ko} = \frac{\tau_p}{\tau_{Ko}} \tag{2.7}$$

where τ_{ko} is the Kolmogorov time scale of turbulence [12]. Loth [13] summarizes each of the Stokes numbers as follows:

Table 2-1: Summary of the classifications of various Stokes numbers summarized from Loth [13]

$\boldsymbol{Stk_f \ll 1}$	Particle motion is weakly affected by the macroscopic fluid motion
$\boldsymbol{Stk_f \gg 1}$	Particle motion is substantially affected by the macroscopic fluid
$\boldsymbol{Stk_L \ll 1}$	Motion of the particle follows integral-scale structures
$\boldsymbol{Stk_L \gg 1}$	Particle motion is weakly affected by the turbulent structures
$\boldsymbol{Stk_{Ko} \sim 1}$	Particle motion substantially modified by Kolmogorov scales
$\boldsymbol{Stk_{Ko} \ll 1}$	Particle motion approximately follows all turbulent structures

2.2.2 Mass Loading

Mass loading is the ratio of the mass flow rate of the particles to the mass flow rate of the fluid:

$$\Omega = \frac{\dot{m}_p}{\dot{m}_f} \tag{2.8}$$

This parameter is very important in turbulence modulation in particle-laden jets. Depending on the size of the particle, an increase in mass loading can increase or decrease the velocity fluctuations of the carrier fluid. Section 2.3 will explain some of the experimental trends, and show how the mass loading affects turbulence modulation.

2.2.3 Particle Size

Depending on the size of the particle, certain characteristics and properties are considered and vary when analyzing particles in a fluid such as Brownian motion and diffusion, lift and drag forces, terminal velocity and gravitational settling, and coagulation. Each of these properties will illustrate the significance of the particle size and will demonstrate how certain properties change with particle size, thus affecting turbulence modulation. The equations and characteristics that are discussed in this section will be particles that are spherical and range between 0.01 – 1000 microns.

2.2.3.1 Brownian Motion and Diffusion

Particles that are smaller than a micron depict strong behavior of Brownian motion. Brownian motion is irregular and random motion undergone by a series of small particles in a medium i.e., a fluid. This is due to the gas-particle interaction on the molecular level. Brownian motion for a small particle suspended in a still fluid is described using the Langevin equation:

$$m_p \frac{dv}{dt} + \frac{3\pi\mu d_p}{C_c} v_p = m_p a(t) \tag{2.9}$$

where v_p is the particle velocity, m_p is the particle mass, d_p is the particle diameter, μ is the dynamic viscosity, C_c is the Cunningham correction factor or slip correction factor, and a(t) is the random acceleration. The random acceleration is due to the impact of the fluid on the particle [14]. In addition to the random acceleration in Equation 2.9, the Cunningham correction factor is one of the key parameters that have an impact on the size of the particle. The reason that it is often referred to as the slip correction factor is that under Stokes law, at the surface of a particle the relative velocity of the gas is zero [15]. When the size of a particle approaches the mean free path of gas, they tend to have very low settling velocities, which results in a slip at the

surface [15]. In the Stokes regime, a correction has to be applied for particles that behave this way. Brownian motion becomes more apparent and intensified when the slip correction factor is greater than one.

The expression for C_c is described as:

$$C_c = 1 + \frac{2\lambda}{d_p}[1.257 + 0.4e^{-\frac{1.1d_p}{2\lambda}}] \quad (2.10)$$

where λ is the molecular mean free path. This equation also includes the effects of drag and noncontinuum effects [14]. Table 2-2 shows the relationship between the Cunningham correction factor and the particle diameter. It also shows that once the particle size falls below the micron level, C_c increases by an order of magnitude for each magnitude decrease of the particle diameter. A one-micron particle has a slip correction factor of 1.176. This indicates that the particle settles 17.6% faster than predicted [15]. If Equation 2.9 did not include this term it would be highly inaccurate. The slip correction factor should be used for particles that are smaller than 5 microns, for greater accuracy [15].

Table 2-2: Variations of Cc with particle size for a λ=0.07 [7]

Particle Size, μm	Cunningham Correction Factor, C_c
10	1.018
1	1.176
0.1	3.015
0.01	23.775
0.001	232.54

Diffusion, in relation to particles, is the kinetic energy of particles in a concentration gradient. The concentration of particles flow from an area of high concentration to one of low concentration. The diffusion coefficient, D, is used to describe Fick's first law of diffusion in one spatial gradient, which is defined as:

$$J = -D\frac{dn}{dx} \tag{2.11}$$

where J is the flux of the particles and $\frac{dn}{dx}$ is the concentration gradient. As the diffusion coefficient increases, Brownian motion becomes strong and apparent which results in higher mass transfer for the concentration gradient [15]. The Stokes-Einstein equation describes the diffusion coefficient for particles:

$$D = \frac{k_B T C_c}{3\pi \upsilon d_p} \tag{2.12}$$

where k_B is the Boltzmann constant, T is the absolute temperature, and υ is the kinematic viscosity. It is important to note the relationship that the diffusion coefficient has with the

particle diameter. Diffusion has an inverse relationship to particle size. As the particle diameter increases, the diffusion coefficient decreases. Particles at the submicron level behave similarly to the molecules of gas and as a result, gas molecules constantly bombard the particle [16]. The bombardments result in a relatively high diffusion coefficient for small particles [16]. However, as the particle size increases the relative velocity of the gas on the particle becomes zero and thus diffusion decreases [15]. Particles larger than 10 microns are assumed to have a negligible effect on the diffusion coefficient [15]. The diffusion coefficient of a particle is also equal to the kinetic energy in a concentration gradient [15].

2.2.3.2 Lift and Drag Forces

When a particle moves in a fluid, resistance and shear forces such as lift and drag act upon it. For small Reynolds numbers, i.e. $Re_p < 1$, spherical particles obey Stokes drag law:

$$F_D = \left(\frac{1}{2}\right) \rho C_D u^2 A \tag{2.13}$$

where

$$C_D = \frac{24}{Re_p} \tag{2.14}$$

where ρ is the fluid density, C_d is drag coefficient, u is the speed of the particle relative to the fluid, and A is the cross section of the particle. Equation 2.13 is the culmination of both the net and frictional component of the drag force acting on the particle. As the Reynolds number deviates from 1, growing larger, the inertia of the fluid increases [16]. This results in an inaccurate prediction of Stokes drag law [16]. To obtain accurate drag coefficients for $1 < Re_p < 10^3$, the transitional regime developed by Clift [17] must be implemented.

$$C_D = \frac{24[1+0.15Re^{0.687}]}{Re_p} \quad (2.15)$$

The flow moves into Newton's regime when $10^3 < Re_p < 2.5x10^3$. In this regime, the drag coefficient stays constant around 0.44 [18]. Once the Reynolds number exceeds $2.5x10^3$, the drag coefficient experiences a sharp decline due to the transition of flow from laminar to turbulent [18]. Drag forces are apparent where there is a relative velocity between the particle and the surrounding fluid [16]. There are restrictions and limitations for using Equations 2.14 and 2.15. For particles that are tightly packed, or within close distances to surrounding particles, the drag forces are very weak and thus considered negligible [17]. The particle must be spherical and moving at the terminal settling velocity [17]. Indoor aerosols are usually within the Stokes regime, i.e., $Re_p < 1$ [15].

2.2.3.3 Terminal settling velocity and gravitational settling

Terminal settling velocity of particles is achieved when the drag force of the fluid is equal to the gravitational force. This velocity is obtained almost instantaneously in the fluid and when it is reached, the acceleration of the particles becomes zero [15]. Table 2-3 outlines how the settling velocity is obtained, depending on the Reynolds particle number and particle size. When the Reynolds particle number is laminar ($Re_p < 1$), the settling velocity equation does not change with the particle size; this is because the particle is in the Stokes regime. The settling velocity equation has the slip correction factor included; this parameter does vary based on particle size (see section 2.2.3.1 for more discussion about Cunningham correction factor). When the particle size is larger than 10 microns, the Cunningham correction factor is approximately one and thus not included for large particles. When the particle Reynolds number

falls between 1 and 1000, the settling velocity cannot be obtained explicitly, but from an implicit empirical equation:

$$V_S = \left(\frac{\eta}{\rho_g d_p}\right) \exp\left(-3.070 + 0.9935J - 0.0178J^2\right) \tag{2.16}$$

where J is defined as:

$$J = \ln[C_D(Re^2)] = \ln\left(\frac{4\rho_p \rho_g d_p^3 g}{3\nu^2}\right) \tag{2.17}$$

and C_D is defined in Table 2-3. The particle Reynolds number is in the transition regime and the drag coefficient varies greatly so it must be calculated iteratively. When the particle Reynolds number is fully turbulent, the drag coefficient remains steady at 0.44. The equation to obtain the settling velocity is listed in Table 2-3. Observing Table 2-3 one may observe that there are no equations for the cases in which the Re_p >1 for submicron particles. This is because submicron particles are in the Stokes region and the settling velocity is not dependent on the flow conditions but the Reynolds number around the sphere. In other words, the submicron particles are in the Stokes regime and the particle Reynolds number cannot be greater than one due to their size.

Table 2-3: Relationship between the particle size and Settling Velocity Equations

Particle Size	Particle Reynolds Number	Settling Velocity	Cunningham Correction Factor/ Drag Coefficient
$< 0.1\ \mu m$	$Re_p < 1$	$V_{TS} = \frac{\rho_g d^2 C_c g}{18\nu}$	$C_c = 1 + \frac{\lambda}{d}\left[2.34 + 1.05 \exp\left(-0.39\frac{d}{\lambda}\right)\right]$
$0.1\ \mu m - 1\ \mu m$	$Re_p < 1$	$V_{TS} = \frac{\rho_g d^2 C_c g}{18\nu}$	$C_c = 1 + \frac{2.52\lambda}{d}$
$> 1\ \mu m$	$Re_p < 1$	$V_{TS} = \frac{\rho_g d^2 C_c g}{18\nu}$	$C_c \cong 1$
$> 1\ \mu m$	$1 < Re_p < 10^3$	See equation (2.14-2.15)	$C_D = \frac{4\rho_p d_p g}{3\rho_g V_{TS}^2}$
$> 1\ \mu m$	$10^3 < Re_p < 2x10^5$	$V_{TS} = \left(\frac{4\rho_p d_p g}{3C_D \rho_g}\right)^{\frac{1}{2}}$	$C_D = 0.44$

In addition to the Reynolds particle number, a particle's size also has a significant impact on the terminal velocity and the time in which it settles. Table 2-4 shows the settling velocity and the time it takes to settle 0.1 meters. As the particle size increases, the settling velocity increases and the settling time decreases. A particle that is 1 micron has a settling velocity of about $3x10^{-5}$ m/s and it takes 55 minutes to settle 0.1 m. A particle that is 100 microns has a settling velocity of about 0.30 m/s and takes 0.33 seconds to settle 0.1 m. Observing the trend in Table 2-4, as the particle size increases an order of magnitude, there is a decrease in settling time by two orders of magnitude.

Table 2-4: Settling velocity at standard temperature and pressure [19]

Particle Size, μm	Settling velocity, m/s	Time to settle 0.1 m
0.01	$6.92x10^{-8}$	401 hrs
0.1	$8.82x10^{-7}$	31.5 hrs
1	$3.48x10^{-5}$	48 min
10	$3.06x10^{-3}$	33 sec
100	$2.49x10^{-1}$	0.4 sec

2.2.3.4 Coagulation

Coagulation is the process by which two particles collide to form one larger particle. There are two main types of coagulation: thermal and kinematic. Thermal coagulation is due to the randomness of Brownian motion. Kinematic coagulation occurs from particle motion due to the forces of gravity, electrical forces or aerodynamic effects [15]. This phenomenon is important because it decreases the overall concentration of the particles with time. The equation that describes thermal coagulation is described as:

$$\frac{dN}{dt} = -K_0 N^2 \tag{2.18}$$

where K_0 is the coagulation coefficient, N is the number of particles in a volume or concentration, and $\frac{dN}{dt}$ is the rate is at which the number of particles change with time. This equation shows that the rate of coagulation is directly proportional to the number of particles in

the concentration squared [15]. This equation is only applicable to monodisperse spherical particles.

$$K_0 = \frac{4kTC_c}{3\mu} \; for \; d_p \; > \; 0.1 \; \mu m \tag{2.19}$$

K_0 depends on the size of the particle because the Cunningham correction factor is included in the equation, which is particle size dependent. Table 2-5 shows how the coagulation coefficient influences the particle size. The parameter K is the corrected coagulation coefficient. It is obtained by multiplying β by the coagulation coefficient, K_0. If K is implemented, then equation 2.18 can be applied to all particle sizes [15]. As the particle size increases, the value for K increases; however this coefficient starts to level off after one micron. This is due to the correction factor β not changing and because the larger the particle becomes, the less likely the particles will be to collide with each other and stick. The initial concentration for particles in an indoor environment is usually 10^2 per cm^3[15]. According to Hinds et al. [15] the time to half the concentration will be 231 days. Because of this, coagulation will not be included in the author's analysis.

Table 2-5: Coagulation Coefficients at Standard Conditions [15]

Particle Size, μm	Correction Factor, β	K_0, m^3/s	K, m^3/s
0.004	0.037	$168\ x\ 10^{-16}$	$6.2\ x\ 10^{-16}$
0.01	0.14	$68\ x\ 10^{-16}$	$9.5\ x\ 10^{-16}$
0.04	0.58	$19\ x\ 10^{-16}$	$10.7\ x\ 10^{-16}$
0.1	0.82	$8.7\ x\ 10^{-16}$	$7.2\ x\ 10^{-16}$
0.4	0.95	$4.2\ x\ 10^{-16}$	$4.0\ x\ 10^{-16}$
1.0	0.97	$3.4\ x\ 10^{-16}$	$3.4\ x\ 10^{-16}$
4	0.99	$3.1\ x\ 10^{-16}$	$3.1\ x\ 10^{-16}$
10	0.99	$3.0\ x\ 10^{-16}$	$3.0\ x\ 10^{-16}$

2.2.4 Coupling

One-way coupling assumes that the particle interaction with the air is negligible in turbulent flow, but not vice versa. In other words, particles do not influence the continuous phase, but the continuous phase influences the particles. This assumption is useful in many multiphase applications, especially since it reduces computational effort [13]. One-way coupling allows one the ability to calculate the flow field before introducing particles, since it will not be dependent on particle location or velocity [13]. In ANSYS, if one is using the one-way assumption, one does not need to inject the particles into the domain until after the continuous

phase has been calculated. Each coupling regime is defined based on the volume fraction, Φ_p, of the particles which is defined as:

$$\phi_p = \frac{N\dot{V}_p}{\dot{V}} \tag{2.20}$$

where N is the number of particles, $\dot{V}_p$ is the volume of a particle and $\dot{V}$ is the volume of the geometry which occupies both particles and the fluid [11]. Elghobashi et al. [11] introduced this relationship between volume fraction and coupling regimes for particle-laden jets. One-way coupling occurs when $\Phi_p \leq 10^{-6}$. When the volume fraction is this low, the momentum transfer between the particles and the turbulence of the fluid is negligible [11]. In many numerical research studies [19-28] relating to indoor particulate dispersion, one-way coupling is often applied because of low particle loading. In this regime, the particle response time will not have an impact on the turbulence of the fluid.

In two-way coupling, in addition to the fluid influencing the particles, the particle motion also affects or disturbs the motion of the fluid. Two-way turbulence coupling occurs when $10^{-6} \leq \varphi_p \leq 10^{-3}$. When this occurs, the momentum transfer of the particles are great enough to affect the turbulence from the air [11]. In this regime, when the particle response time becomes greater than one the particles decrease and turbulence becomes dominant [11]. As τ_p increases, the particles begin to enhance the production of turbulence [11]. When the particle Reynolds number becomes greater than 400, vortex shedding occurs [11]. On the other hand, when τ_p is decreased, the surface area of the particulate phase increases [11]. This results in a dissipation of turbulence [11].

Four-way coupling uses the two-way coupling criteria in addition to particle-particle collisions. Elghobashi et al. [11] describes four-way coupling as occuring when the volume

fraction, $\varphi_p \geq 10^{-3}$. In this regime, the particle loading is very high. Inter-particle collisions fall under two categories: dilute and dense flow. The Knudsen number is the ratio of the particle response time to the timed average between collisions [29]. The flow is considered dilute when the Knudsen number, Kn, is Kn < 1 and dense when Kn > 1. In dilute flow, the particle-particle collision is smaller than the particle response time [29]. This means that the particles do not have time to respond to the flow [29]. In dense flow, the particle-particle interaction is faster than the particle response time [29]. In this case, the fluid transport of the particles are dominant [29].

2.3 Mechanisms of Turbulent Modulation

Although there has been considerable progress in understanding turbulence modulation, there is still much that is not understood about this phenomenon [30]. Below is a list of mechanisms that can affect the turbulence in a flow-field. The first mechanism states that the mean velocity of the continuous phase can change from the addition of particles in a flow field. One way to identify if this is occurring is to measure the mean flow of the single phase, and import the particles in order to observe any difference [30]. The second mechanism is based on the size of the particles. If the particles are large, wakes can develop behind the particles and result in a change in turbulence modulation. This is based on the volume fraction of the particles in the flow. Crowe et al. [30] points out that the volume fraction is low in most dispersed gas-solid flows. The third mechanism also stems from the result of wakes created by large particles. The fourth mechanism occurs when large particles exert a force due to the large particle response time and high Stokes number. The force that is exerted removes energy from the turbulence of the flow-field [30]. The remaining two are utilized if the particles are considered clouds, thus are not of concern to this study [30].

1. Mean velocity of the continuous phase
2. Large particles
3. Random laminar wakes
4. Extra dissipation from particle-particle collisions
5. Particle concentration in turbulent structures
6. Particle concentration in gravity

2.4 Turbulence Modulation in Particle-Laden Jets: Experimental Trends

2.4.1 Summary of Methods

Many experiments investigate the effects of turbulence modulation in particle-laden jets with varying parameters (jet configurations, loading ratios, and particle sizes). One of the common trends observed in each of these flows is that larger particles increase the turbulence intensity, whereas small particles attenuate it [30]. Gore and Crowe [10] compiled previous research experiments to explain how the turbulence intensity increases and decreases with particles. They determined that a critical parameter in understanding the trend is the ratio of the diameter of the particle to the turbulent length scale, d_p/l_e [10]. When $d_p < 0.1*l_e$, turbulence intensity decreases and when it is greater than 0.1, the turbulence intensity increases [10, 30]. This observation is applicable to many two-phase flow systems.

Table 2-6 outlines some of the major experimental studies conducted, displaying the parameters that can influence the turbulence intensity in the flow-field. Mostafa and Mongia et al. [31] noticed that the glass beads increased both the gas turbulence and anisotropy level. It was also observed that the velocity of the mean particles are uniform over the cross-section of the jet due to mixing [31]. Mergheni and Sautet et al. [32] studied the effects of varying Reynolds numbers on the turbulent modulation of particles. They noticed that when the Reynolds number was very high (Re=11,893), the particles increased the gas turbulence; when the Reynolds number was low (Re=2,839), the particles decreased the turbulence of the gas [32]. It is

important to note that the particles in this study were relatively intermediate and larger particles may not show this same trend. Sheen and Jou et al. [33] studied the effects of particle size on turbulence modulation by observing a wide range of particle sizes and loading ratios. It was observed that for the same mass loading, the rate at which the fluid axial velocity decreased increased with increasing particle size [33]. In other words, the decreasing rate was slower for smaller particles. It was also noted that the rate at which the fluid axial velocity decreased on the centerline was lower for single phase than for two-phase flows [33]. Modaress and Tan et al. [34] developed a method for eliminating cross talk error when using Laser Doppler Anemometry. This helps to eliminate error associated with mean velocity and turbulence intensity that often occurs with LDA's [34]. Crosstalk is an error from the reading of digital experimental tools, and occurs between the two phases [34]. When particles were introduced into the flow, the gas-velocity fluctuations reduced, and were proportional to mass loading [34].

Tsuji and Morikawa et al. [35] studied the effects of coarse particles on turbulent intensity in particle-laden jets. It was observed that, for different loading ratios of the same particle, the turbulence intensity peak decreased as the loading ratio increased [35]. It was also observed that when particles were introduced, the maximum intensity decreased when compared to just single-phase flows [35]. In an earlier study, Tsuji and Morikawa [36] studied two-phase flow in a horizontal pipe with both intermediate and coarse particle sizes. In this study, it was found that with an increasing loading ratio, the air velocity decreased for single and two-phase flows. A uniform velocity profile for the intermediate particle size was also observed [36]. Wang and Zhang et al. [37] studied turbulent modulation in round jets with coarse particles. The study concluded that the turbulence intensity of the coarse particles is very close to that of the single-phase flow [37]. Levy and Lockwood [38] studied the velocity measurements in free

turbulent particle-laden jets. Similar to other studies, it was concluded that the large particles had a higher turbulent kinetic energy than smaller particles [38]. An interesting observation was the spreading rate for the particles was largest for the intermediate particles [38]. This is possibly due to the particle response time and the turbulent diffusion of the momentum of the fluid to the gravity [38]. Jou and Lee [39] studied the effects of mass loading in particle-laden jets. It was concluded that particle mass loading had no effect on axial mean velocity at the exit of the jet [39]. Like similar studies, the smaller particles had turbulence intensities that are lower than that of a single phase jet and decreases with increasing particle loading [39].

Table 2-6: Previous experiments conducted investigating turbulence modulation

Reference	Jet Configuration Type	Fluid	Particle Material	Particle Size (microns)	Particle Density (kg/m3)	Loading Ratio
Mostafa & Mongia (1989) [31]	coaxial jet, vertical downward, D=457 mm	Air	Glass Beads	105	2500	0.2
Mergheni & Sautet (2008) [32]	coaxial jet, round and annular, D=6 mm	Air	Glass Beads	102-212	not mentioned	0.7
Sheen & Jou (1994) [33]	D=15 mm	Air	Polystyrene	210, 460, 780	1020	0-0.36
Modaress and Tan (1983) [34]	D=20 mm	Air	Glass beads	50	2990	0.32, 0.85
Tsuji & Morikawa (1982) [36]	Horizontal, round jet D=30 mm	Air	Plastic Particles	200, 3400	1000	0-6
Wang & Zhang (2009) [37]	Vertical Downward round jet, D=20 mm	Air	Glass Beads	190-1,232	2450	not mentioned
Levy & Lockwood (1981) [38]	Vertical Downward jet, D=15 mm	Air	Sand	215-1060	2620	1.14-3.5
Tsuji & Morikawa (1988) [35]	Vertical downward, round jet D=28 mm	Air	Polystyrene	170-1400	1020	not mentioned
Jou & Lee (1993) [39]	Vertical downward jet	Air	Polystyrene	210, 780	1020	0-0.36

2.4.2 Laser Doppler Anemometry

One of the most popular tools used to measure the turbulence modulation in particle-laden jets is the Laser Doppler Anemometers (LDA). LDA has been popular in use since the successful experimental investigation with Lee and Durst in 1981 [40]. LDA is a non-invasive measuring tool that uses two laser beams, and seeded particles that measures the shift in frequency, to determine the velocity at a specific point in time. It is widely used in measuring turbulence modulation because of its ability to measure turbulent flows in which the fluctuating velocity changes with time [41]. Figure 2-1 shows the set-up of a dual-beam system that measures particle velocity in one direction. Each beam has an equal intensity, which improves the estimate of the Doppler shift. The beams are adjusted so that they intersect, and the measurement volume is where the particles pass so that both beams can be detected. Even though the beams possess equal intensity, the frequency shift from each beam will be different because of their orientation [42]. The frequency shift for both beams becomes:

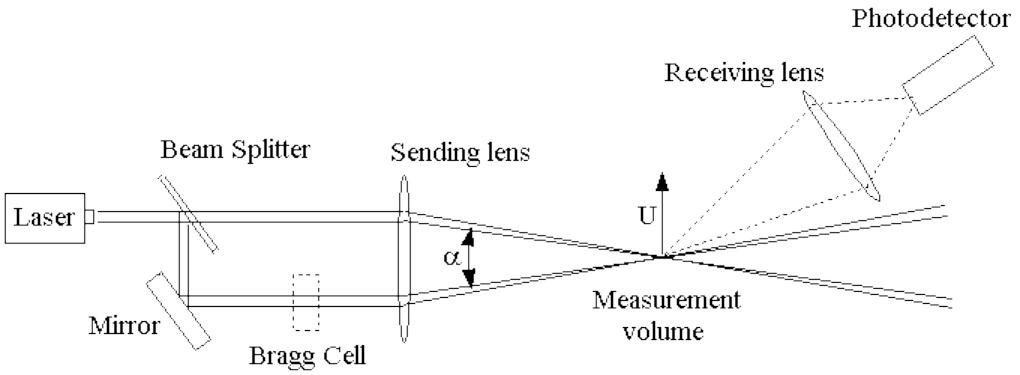

Figure 2-1: Single component dual-beam LDA system in forward scatter mode (used with permission) [42]

$$\frac{|f_{d1}-f_{d2}|}{2} = \frac{2V_{sc}}{\lambda}\sin\left(\frac{\theta}{2}\right) \tag{2.21}$$

where f_{d1} and f_{d2} is the Doppler shift for each beam, V_{sc} is the velocity of the scattered particle, λ_w is the wavelength, and θ is the angle of the intersection between both beams. In the measurement volume section, the interference of the light beam results in light and dark bands called fringes [41]. When particles pass through the measurement volume they go through these fringes and the particle fluctuates based on the amount of light that is scattered [42]. This fringe spacing, d_f, is calculated as:

$$d_f = \frac{V sin\left(\frac{\theta}{2}\right)}{\lambda} \tag{2.22}$$

Some disadvantages to this measurement technique are: the monetary expense, no transparent flow, and the inability to give continuous velocity signals [41]. Often-times, in gas-solid flows, scattered light intensity of the particle diameter is used to distinguish the difference between the gas and solid phases [43]. Particles that are on the submicron level exhibit similar characteristics as gas because their mean free paths are similar. The solid particles must be much larger than the seeded particles to distinguish the difference. The disadvantage to this method occurs when the larger particles travel near the edge of the measurement volume section they are often interpreted as seeded particles [43]. To reduce the chances of this occurring, it is useful to have large differences in the velocity of the seeded particles and the larger particles [43]. Another method of distinguishing between the two phases is through the use of Phase Doppler Anemometry (PDA). PDAs have a larger aperture that can detect small particles with greater accuracy [44]. It also works well for dense particle-laden flows [44].

2.4.3 Particle Image Velocimetry

Particle Image Velocimetry (PIV) has been used in a wide range of applications: microfluidic devices, flows in artificial heart valves, thermal turbomachinery, and fuel injection

spray, just to name a few. Like LDAs, PIV is also a non-invasive tool that measures the instantaneous velocity of particles with seeded tracer particles in the flow. The major difference between LDA and PIV is PIV's ability to measure two or three-dimensional vector fields [45]. LDAs are only able to measure at one point, and in one direction [45]. PIV also requires the use of a high-speed camera to obtain still images of the flow. A disadvantage with the optical tool PIV is its inability to measure in the direction of flow coming toward the camera; Stereoscopic PIV (use of two cameras to obtain third dimension) will have to be used to alleviate this issue [45]. Another difficulty with using this technique is in capturing the small particles in dim light and the larger particles in bright light [30]. If the particles are not in focus, interphase crosstalk will occur [30]. There are techniques that are used to avoid interphase crosstalk, but they are only applicable to volume fractions below 0.01% [30].

2.5 Turbulence Modulation in Particle-Laden Jets: Analytical Trends

Analytical models are useful in predicting the physical behavior of a system in many ideal cases and can be used to validate numerical work. The disadvantages of only utilizing analytical models are the limitations that occur. Below is a summary of the major models that have been developed in relation to turbulence modulation in particle-laden jets and some of the limitations associated with them.

Yuan and Michaelides [46] developed a simple mechanistic theory for turbulence modulation in particle-laden jets for a single particle with eddies. This model focuses on two mechanisms of turbulence production and enhancement: 1) dissipation of an eddy and 2) flow velocity due to the wake of particles [46]. The change in the total time-average of the turbulent kinetic energy was defined as:

$$\Delta E_t = \frac{12\Delta E_k m^*}{\pi d_p^3 \rho_p v_{ed} v_p} = \frac{12\Delta E_k m^*}{\pi d^3 \rho_p v_{ed}(v_{ed} - V_{rel})} \tag{2.23}$$

where m* is the local loading, ΔE_k is the average kinetic energy modification and V_{rel} is the relative velocity of the particle and fluid [46]. If $V_{rel} = 0$ in this model, then no turbulence modification occurs since the volumetric concentrations are very low, i.e. under 1% [46]. ΔE_t represents the summation of the averaged turbulent kinetic energy over time. Although this model provides an easy means of obtaining the turbulent kinetic energy, there are some limitations within this analytical model. One such limitation is the model not working if the relative velocity is zero and is limited to low concentration numbers. Another limitation is that this model is only applicable to a single particle, which is not helpful in many particle-laden flows.

Rizk and Elghobashi [47] developed a two-equation, low Reynolds turbulence model for dilute two-phase flows. This model is modified from Elghobashi and Abou-Arab et al. [48] for high Reynolds number flows now considering the effects of viscous diffusion on the wall. The equations developed in this model include the total effective viscosity (including molecular viscosity), Saffman's lift force, and particle drag which has been altered for the wall [47]. Tsuiji et al. [49] and Maeda et al. [50] were used to validate most of the model parameters [47]. The use of a "hypothetical two-phase flow", due to the lack of experimental data near the wall can be considered an issue with this model. Experimental data in near-wall flows needs to validate the analytical model.

Kenning and Crowe [51] developed an expression to predict turbulence intensity for gas-particle flows. The expression shows the importance of interparticle spacing in developing a turbulent length scale [51]. The equation is expressed below:

$$\frac{\sigma-\sigma_i}{\sigma_i} = \left[\frac{L_h}{L_i} + \frac{L_h}{k_i^{\frac{3}{2}}}\frac{f\left(\bar{v}-\bar{v}_p\right)^2}{\tau_d}\left(\frac{\rho_d}{\rho_G}\right)\right]^{\frac{1}{3}} - 1 = TM \tag{2.24}$$

where the left hand side represents the fractional change in turbulence intensity, L_h is the hybrid length scale, L_i is the interparticle spacing, ρ_d and ρ_G represents the bulk densities for the particle and gas phase, and second term inside the brackets on the right hand side is the turbulence modulation parameter, TM [51]. The other terms in this equation $\bar{v}$, $\bar{v}_p$, f, k_{in} represent the mean velocity of the fluid, mean velocity of the particle, the ratio of the particle drag to the Stokes drag, and the inherent kinetic energy respectively [51]. This equation says that the turbulence will increase if $L_h < L_i$ [51]. One issue with this model is the assumption that the production term and the particle free flow are the same [52].

Kim and Lee et al. [52] developed a model for the turbulence modulation in a wide range of two-phase flows that are considered dilute. In the simple model described in Yuan and Michaelides [46] only the wakes behind particles and dissipation of turbulent kinetic energy were considered. In Kim and Lee's model they also consider drag forces within each phase [52]. Although compared to other models [9, 51, 53], when the RMS is low the error is still high, around 16% [52]. This model is based off the mixing length theory, which assumes equilibrium flow [52].

Yarin and Hetsroni [9] developed an analytical model to show the effects of polydispersion and turbulence intensities in two-phase flows. This model will be discussed in detail in Chapter 3, and will be modified with the author's research in Chapter 5.

2.6 Turbulence Modulation in Particle-Laden Jets: Numerical Trends

2.6.1 Particle Tracking Methods

There are two general approaches to modeling the particles, and the fluid(s) containing them – the Eulerian and the Lagrangian method. The method in which the particle phase acts as a continuum, and the conservation equations for the fluid and the particle are utilized is known as the Eulerian method. The method in which the particle phase is considered discrete and tracked individually is known as the Lagrangian method. The fluid phase is treated as a continuum for this method. The equation used for the Lagrangian approach will be explained in Chapter 4. This section will outline some of the research conducted using each of these particle-tracking methods, and some of the advantages and disadvantages of each method.

2.6.1.1 Eulerian Method

The Eulerian multiphase model can be used to model many phases that interact with each other [54]. Depending on the application of the two-phase flow system the Eulerian particle-tracking model can yield accurate results and save computational time, compared to the Lagrangian method. This model works well for fine particles that are subject to constant velocity fluctuations of the continuous phase [55]. There are two ways in which the surface forces of the particles are modeled: mixed fluid and separated fluid. The mixed fluid approach makes the assumption that the relative velocities between the fluid and the particles are negligible [30]. In this approach, there is only one set of momentum conservation equations instead of the two (dispersed and continuous phase equations) [30]. The separated fluid model, also known as the two fluid method, makes the assumption that the fluid and particle phase are separate but interpenetrating continua [30].

2.6.1.2 Lagrangian Method

The Lagrangian model individually tracks and calculates each path that a particle travels, along a trajectory. One of the major differences in this method, when compared to the Eulerian model, is that each of the properties (velocity, concentration, etc.) changes as the particle travels on the path [30]. With the Eulerian model, the properties are averaged in a grid that is fixed [30]. Within the Lagrangian model, there are two ways in which the surface forces on the particles can be treated: point force or resolved surface treatment. In point force, the particle is at a specific point in the flow and travels with a unique velocity, and the continuous phase is Eulerian [30]. Whereas, the resolved surface treatment information around the particle is of interest, and must be highly resolved [30]. A disadvantage of the resolved surface treatment is the low limit (less than a hundred) of particles that can be resolved in a flow field [30].

2.6.2 Turbulence Models

Turbulence is a space and time dependent chaotic phenomena characterized by the increase in vortices and strain. Mathematically, it is described using the Navier Stokes equations, which are essentially the conservation of momentum and viscous stresses. In CFD, there are many models that directly calculate or approximate the Navier Stokes equations, i.e. Reynolds stresses to describe the turbulence for a given flow-field. The three ways to model turbulence are Reynolds Averaged Navier Stokes (RANS), Direct Numerical Simulations (DNS), and Large Eddy Simulations (LES).

In the Reynolds Averaged Navier Stokes (RANS) based turbulence models, there are three main ways in which turbulence can be approximated: Linear eddy viscosity models, nonlinear eddy viscosity models, and Reynolds Stress Models (RSM) [56]. The main difference

between these models is the way the eddy viscosity is calculated in a linear or nonlinear way. The RSM does not use the eddy viscosity assumption, but calculates the Reynolds stresses directly. RSM is computationally expensive since it has to solve 6-8 equations simultaneously. The two equation models, such as the *k*-ε models, are widely used because of their wide range of engineering applications and computational efficiency. Shih and Liou et al. [57] developed the realizable *k*-ε model, greatly improving upon the standard *k*-ε model for a wide range of flows including: rotating homogeneous flows, boundary shear flows, channel flows, and backward facing step flows. Yan [55] modified the *k*-ε equations successfully to consider the effects of wakes for large particles. This model was compared to experimental data using vertical and axi-symmetric jets [55].

With DNS, no turbulence models are required because the Navier Stokes equations are solved directly [56]. With this method all of the large (integral scales) and small scales (Kolmogorov scales) have to be resolved [56]. This method is the most numerically accurate way to calculate the Navier Stokes equations. The disadvantage with this model is that it is computationally expensive and typically not used in large and complicated geometries. The number of nodes required to solve a DNS simulation is proportional to Re^3 [56]. Currently, DNS is used for low Reynolds number flow applications. An extensive study using DNS came from Ling and Chung et al. [58]. Ling and Chung et al. [58] used a pseudo-spectral method and Lagrangian method to study the effects of two-way momentum-coupled interaction between particles and the mixing layer [58]. One result concluded from this study was that the turbulent kinetic energy decreased at intermediate Stokes numbers [58]. It was also observed that the turbulent kinetic energy increased when particles with small Stokes numbers were considered [58]. These results applied to a mass loading of 0.3 [58].

In the LES, the large scales are directly calculated and the small scales are modeled using subgrid-scale models (SGS). Yeoh describes the purpose of SGS models as a means of indicating the losses associated with the kinetic energy [59]. These losses are caused by viscous forces, and only account for the SGS stresses statistically rather than accurately [59]. A problem with LES is that SGS models do not associate changes in the Reynolds number or flow type without tuning the model [60]. Almeida and Jaberia [61] developed a new SGS model for round particle-laden jets and concluded that this model accurately showed the effects of two-way coupling of the particles and the gas [61]. They concluded that when heavy particles were added to the flow the centerline velocity decreased at a slow rate and increased the overall turbulence intensity [61].

2.7 Summary of Literature and Relevance of This Research

In the literature, many experimental studies investigating turbulence intensity in particle-laden jets were examined. However, there are not many studies considering the effects of polydispersion with turbulence intensity. The analytical models that have been discussed also do not show the importance of polydispersion except that of Yarin and Hetsroni [9], which in this study will show that it is not realistic for experimental or numerical applications. This research will modify the analytical model developed by Yarin and Hetsroni [9] that can be applied to a realistic particle-laden jet and compare it to the numerical model used in CFD.

Chapter 3: Modified Prandtl Mixing Length Theory

This chapter will explain the modified Prandtl mixing length theory developed by Yarin and Hetsroni [9]. This mixing length theory has been modified to account for viscous interaction of small particles, and the continuous phase. This analytical model is applied to turbulent polydisperse particle-laden flows that are classified as dilute. This chapter will provide a summary of the analyses by Yarin and Hetsroni [9].

3.1 Assumptions in the Theory

The main assumptions outlined in this modified mixing length theory are summarized below:

1. Steady incompressible turbulent flows are polydisperse
2. The particle Reynolds number for all particles must be less than 110 ($Re_{p,crit} < 110$)
3. Transverse pressure gradients are considered negligible
4. Particles and continuous phase travel at different velocities
5. Average velocity between the particles and the continuous phase are negligible
6. Particles do not exit the domain and persist together during their life time
7. Particles travel in an inviscid fluid

The incompressible assumption means that the density of the fluid remains constant throughout the process. The second part of this assumption, which states that the particles are polydisperse, in this case means that they are of different sizes and densities. For example, particle size 1 will have a different diameter and density than particle size 2. In the second assumption, it is stated that the critical particle Reynolds number must be less than 110. This is to avoid wake effects that normally occur for large particles or particles that are travelling at very high speeds. Section 3.2 addresses how the critical particle Reynolds number is calculated. It is important to note that Re_{pcrit} is different than Re_p. Re_{pcrit} is the particle Reynolds number based

solely on the initial fluctuating velocity of the continuous phase and this value must be less than 110 to ensure that the limit of $(1+\gamma)^{-1}$ is met. The particle Reynolds number indicates the Reynolds number around the spherical particles. The third assumption mentions disregarding transverse pressure gradients. This includes pressure gradients associated with boundary layers and pipe flows. The fourth assumption states that the particles and the fluid travel at different velocities. This is a typical assumption and is applied to many particle-laden flows. The fifth assumption occurs only in fully developed turbulent flows. The sixth assumption states that the particles are not to exit the domain, but spend the entire time in the control volume. Depending on how the domain is set up and how the boundary conditions are defined, one can also meet this assumption to ensure that most particles remain in the control volume. The last assumption talks about the fluid being inviscid. Yarin and Hetsroni [9] justify this assumption by stating that the size of the fluid element is much larger than the particle [9].

3.2 Theory and Equations

The continuous phase and the particle motion are both described using the conservation of momentum equation:

$$d[v' + \sum_{i+1}^{n} \gamma_i v_i'] = 0 \tag{3.1}$$

$$\frac{m_i dv_i'}{dt} = \frac{1}{2} C_D^i f_i \rho \tilde{v}_i |\tilde{v}_i| \tag{3.2}$$

where the *v'* is the fluctuational velocity of the air, v_i', particle fluctuational velocity, m is the mass of the fluid, γ is the mass content of the particles in the fluid, ($\gamma = M_p/M$), where M is the mass of the fluid in the entire domain and M_p is the mass of the particles. Equation 3.2 states that the change of the momentum is equal to the drag force exerted from the fluid. The initial conditions for equations 3.1 and 3.2 are $v' = v'_0$ and $v'_i = 0$. Where v'_0 is the initial fluctuating

velocity of the air. When equation 3.1 is integrated and expressed in dimensionless form, one obtains:

$$[v^{'} + \sum_{i+1}^{n} \gamma_i v_i^{'}] = 1 \tag{3.3}$$

where $\bar{v}' = \frac{v'}{v_0'}$ and $\bar{v}_i' = \frac{v_i'}{v_0'}$.

Assuming Stokes drag law, $C_{Di} = \frac{24}{Re_i}$ for the particles, equation 3.2 can now be expressed as:

$$\frac{dv_i'}{dt} = \left(\frac{1}{2}\right) \rho \frac{24}{\tilde{v}_i d_i} v \tilde{v}_i |\tilde{v}_i| \dot{V}_i / m_i) \ = \frac{18\mu\tilde{v}_i}{d_i^2 \rho_i} \tag{3.4}$$

where $\dot{V}_i$ is the volume of a sphere. When equations 3.1 and 3.4 are combined the result is:

$$\frac{d\tilde{v}_i}{dt} = \tau_i^{-1}[1 - \sum_{i=1}^{n} \gamma_i \bar{v}_i' - \bar{v}_i'] \tag{3.5}$$

where the particle response time or the relaxation time can be calculated as:

$$\tau_i = \frac{d_i^2 \rho_i}{18\mu} \tag{3.6}$$

Combining equations 3.1 and 3.5 to consider a mixture containing two particle sizes, i.e., bidisperse, the result is:

$$\bar{v}' + \gamma_1 \bar{v}_1' + \gamma_2 \bar{v}_2' = 1 \tag{3.7}$$

$$\frac{d\bar{v}_1'}{dt} = \tau_1^{-1}[1 - (1 + \gamma_1)\bar{v}_1' - \gamma_2 \bar{v}_2'] \tag{3.8}$$

$$\frac{d\bar{v}_2'}{dt} = \tau_2^{-1}[1 - \gamma_1 \bar{v}_1' - (1 + \gamma_2)\bar{v}_2'] \tag{3.9}$$

where the indexes of 1 and 2 are the large and small particles respectively, and when time = 0: $\bar{v}' = 1,\ \bar{v}_1{}' = \ \bar{v}_2{}' = 0$

Integrating equation 3.8 and 3.9 results in:

$$\bar{v}_1{}' = (1+\gamma)^{-1}\{-(\varphi_2-\varphi_1)^{-1}[\gamma_1^{-1}(1+\gamma)-\phi_2][\gamma_1^{-1}(1+\gamma)-\varphi_1]\exp(-\gamma_1\varphi_1\bar{\tau}^*) + (\varphi_2-\varphi_1)^{-1}[\gamma_1^{-1}(1+\gamma)-\varphi_1][\gamma_1^{-1}(1+\gamma)-\varphi_2]\exp(-\gamma_1\varphi_2\bar{\tau}^*)+1\} \quad (3.10)$$

$$\bar{v}_2{}' = (1+\gamma)^{-1}\{(\varphi_2-\varphi_1)^{-1}[\gamma_1^{-1}(1+\gamma)-\phi_2]\exp(-\gamma_1\varphi_1\bar{\tau}^*) - (\varphi_2-\varphi_1)^{-1}[\gamma_1^{-1}(1+\gamma)-\varphi_1]\exp(-\gamma_1\varphi_2\bar{\tau}^*)+1\} \quad (3.11)$$

where:

$$\varphi_{1,2} = 0.5\{\gamma_1^{-1}[(1+\gamma_1)\omega+(1+\gamma_2)] \pm \sqrt{\gamma_1^{-2}\{[1+\gamma_2)-(1+\gamma_1)\omega]^2\}+2\omega\gamma_1^{-1}\gamma_2}\} \quad (3.12)$$

where $\omega = \frac{d_2^2}{d_1^2}$ and the dimensionless time $\bar{\tau}^*$, is defined in equation 3.13, where τ^* is the characteristic time.

$$\bar{\tau}^* = \tau^*/\bar{v}_1 \quad (3.13)$$

$$\tau^* = 36\left(\left(\frac{\bar{l}}{\bar{\rho}}\right).Re_{p,crit}\right) \quad (3.14)$$

$$Re_{p,crit} = d_2|v_0'|/\nu \quad (3.15)$$

The dimensionless relaxation time, $\bar{\tau}^*$, is a very important parameter in this analysis because if the characteristic time, τ^*, is not much greater than 1 the particles will not reach the limit of $(1+\gamma)^{-1}$. This does not mean that the Stokes number needs to be very small. One can still have a relatively large Stokes number, and this limit will still be reached provided $\tau^* \gg 1$. This and other criteria such as using the ratio of particle sizes, particle densities, and the critical particle Reynolds number must hold for this assumption to be true.

Figure 3-1 shows how the turbulence intensity of the air, large and small particles change with the characteristic time, τ^*. Initially the air has a high turbulence intensity and as the particles and air begin to mix and transfer momentum eventually a point is reached in time in which the turbulence intensities are in equilibrium. In this Figure, the point is reached when $\tau^* = 5$ for all mass contents. This figure shows the cases when the mass contents, γ=0.25, 0.75

and 1.75. For the turbulent intensity of air, the mass contents decrease as the turbulence intensity decreases and for the particles the opposite trend is occurring. As the mass contents increase, the rate at which the turbulence intensity decreases is more pronounced. The limit is reached sooner in the characteristic time for larger mass content values. This is due to the larger density values which results in a higher momentum transfer when compared to the smaller mass content values.

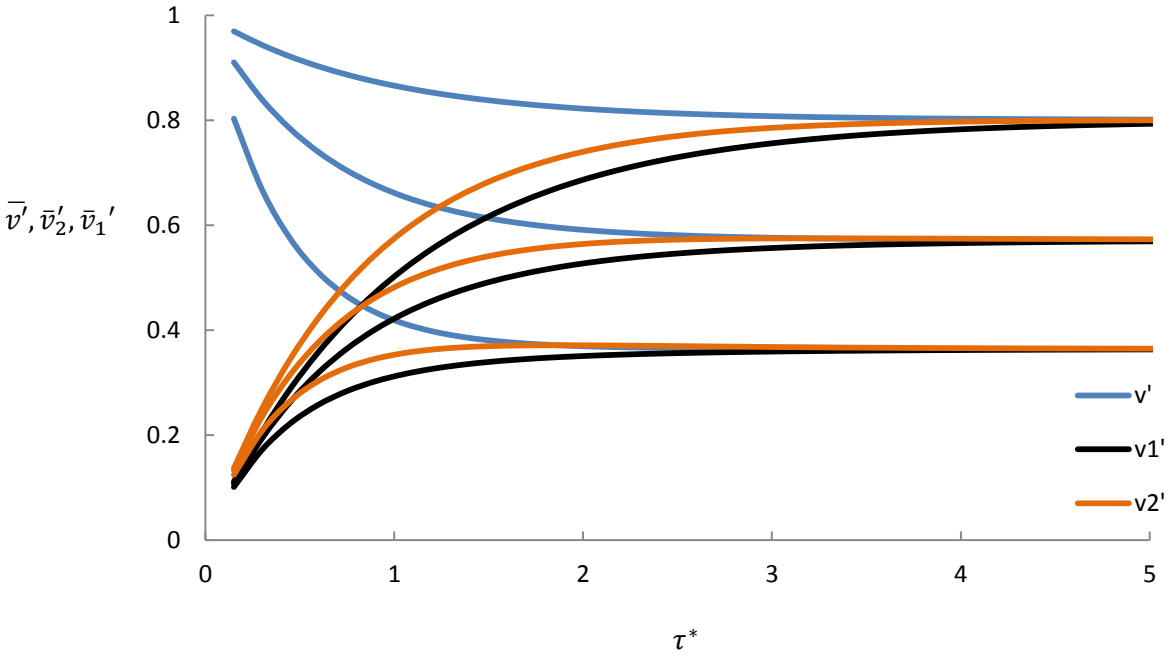

Figure 3-1: Turbulence intensity of air, large and small particles as a function of characteristic time at γ=0.25, 0.75, and 1.75 and ω=0.8

3.3 Results by Yarin and Hetsroni [9]

Figures 3-2 through 3-4 were generated using equations 3.7, 3.10-3.12. Each of these figures were recreated from Yarin and Hetsroni's [9] study using Microsoft Excel. It is important to note that these plots are all based on the assumption that the particles are in Stokes drag regime. Chapter 5 will display the results from the author's CFD analysis as well as a

modified version of this analytical model with the transitional drag inserted into the momentum equation, to show how the drag changes the behavior of Figures 3-2 through 3-4.

Figure 3-2 shows the effect of how varying the mass content influences turbulence intensity for large, $\bar{v}_1'$, and small, $\bar{v}_2'$, particles. As the particles increase in mass content, the turbulence intensities of both the carrier fluid and the particles decrease. When the dimensionless interaction time is much greater than 1, the limit, $(1+\gamma)^{-1}$, is always reached, as displayed in Figure 3-2. As the carrier fluid's turbulence intensity, $\bar{v}'$, decreases, the large and small particles turbulence intensity, $\bar{v}_1$ and $\bar{v}_2$ respectively, increases in the flow-field. This is due to the momentum transfer that is taking place as the air and particles interact. Both large and small particles begin with very low turbulence intensities and increase with time until they approach a limit of $(1+\gamma)^{-1}$. The carrier fluid starts with a high turbulence intensity and gradually decreases with time and starts to exchange the momentum with the particles. The dimensionless relaxation time is not shown on this graph because it is embedded in equations 3.10a and 3.10b to calculate $\bar{v}_1'$ and $\bar{v}_2'$.

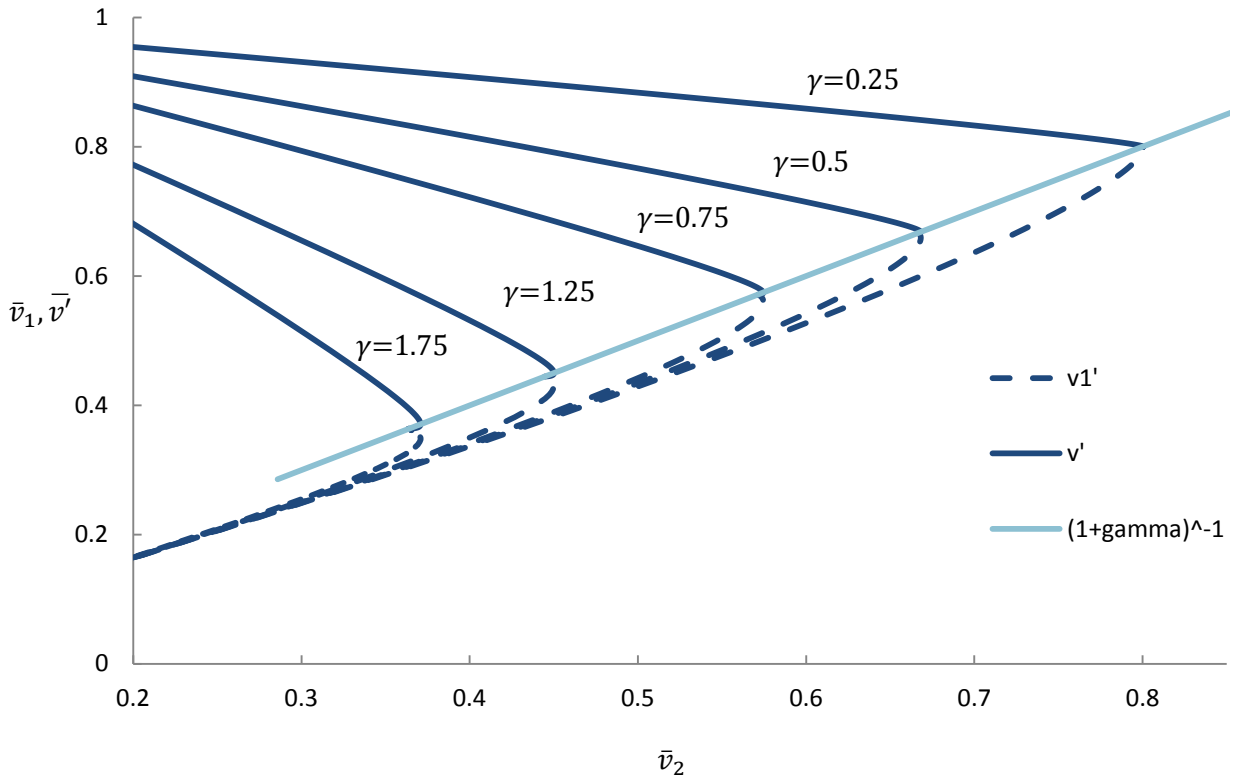

Figure 3-2: Turbulence intensity of large ($\overline{\boldsymbol{v}_1}'$) and small ($\overline{\boldsymbol{v}_2}'$) particles with varying mass contents (ω=0.8, γ1=γ2=γ/2)

Figure 3-3 shows the effect of varying mass content values on turbulent intensity. In Figure 3-2, the mass content of the large particle was equal to that of the small particle. In this figure, they are not equal. m_c=0.25 means that the mass content of the large and small particles, γ1 and γ2 are equal to 0.2 and 0.8 respectively. This graph shows that the slope stays constant, and the turbulence intensity does not change significantly for drastic mass content values. Yarin and Hetsroni [9] point out that the small particles decrease in mass content from m_c=0.25 to m_c=2, and this results in a decrease in the energy dissipation [9].

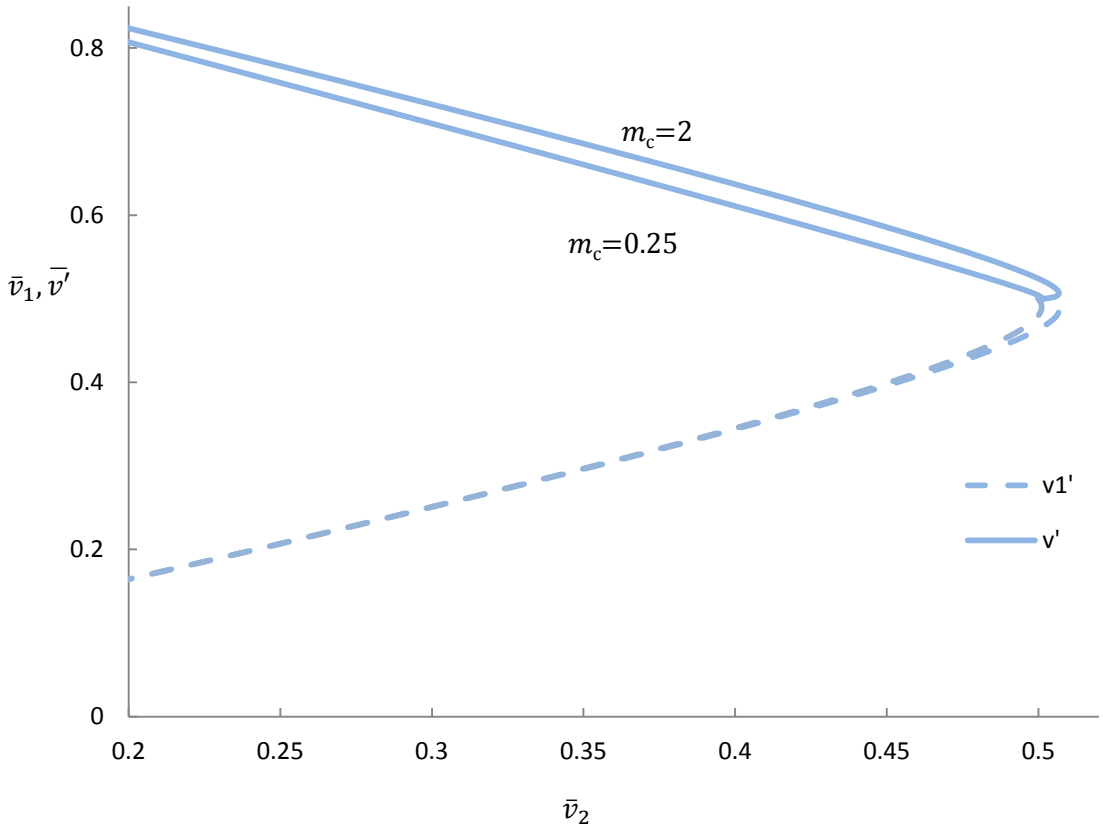

Figure 3-3: Turbulence intensity of large ($\overline{\boldsymbol{v}_1}'$) and small ($\overline{\boldsymbol{v}_2}'$) particles with varying mass contents ratios (ω=0.8, γ=1)

Figure 3-4 shows how particle size ratios, ω, vary with turbulence modulation. As the particle size ratio, ω, increases, the turbulence intensity of the air decreases and the intensity of the large particles increases. This trend follows many other previous studies done with large monodisperse particles [30]. Observing this figure in this regime, the effects of intensity grow larger in difference, and using the monodisperse assumption for Stokes flows may not be accurate when calculating turbulence intensity.

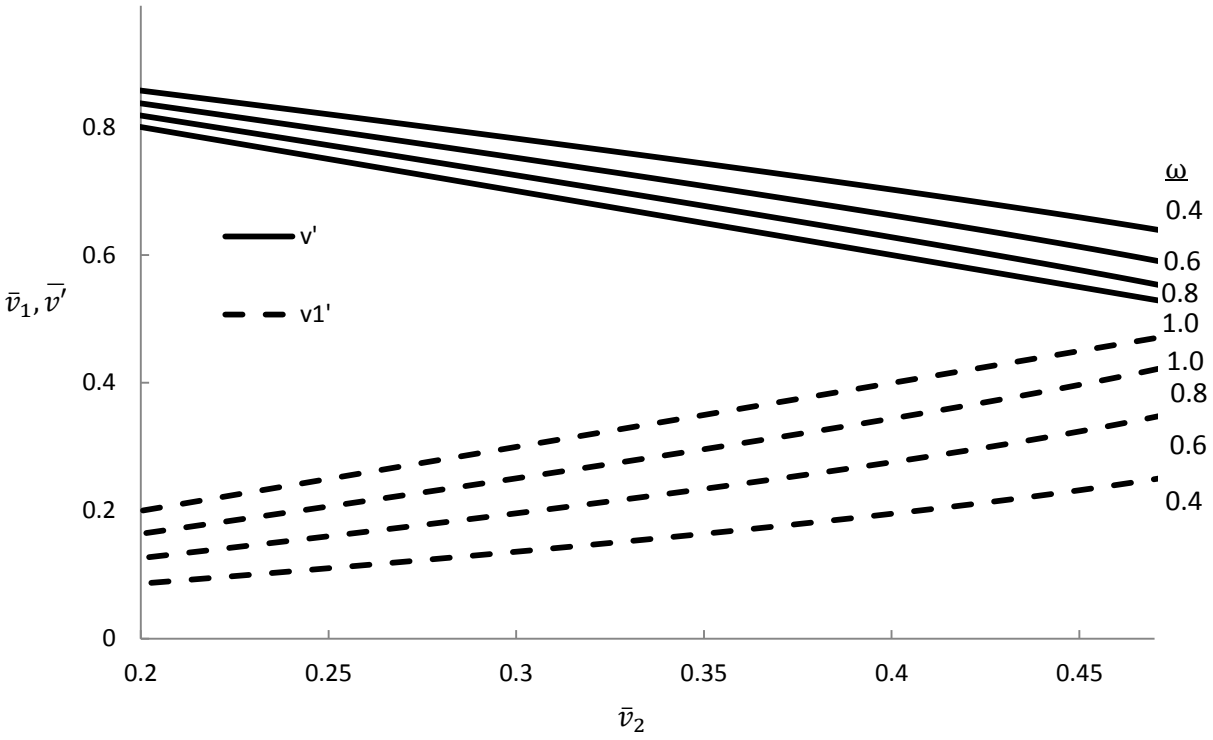

Figure 3-4: Turbulence intensity of large ($\overline{\boldsymbol{v}_1}'$) and small ($\overline{\boldsymbol{v}_2}'$) particles with varying particle size ratios ($\gamma 1=\gamma 2=\gamma/2=0.5$)

Figure 3-5 shows the effect of varying the characteristic time, τ^*, on the mass content values, γ, for a bidisperse mixture. At a low characteristic time, one can see that the carrier fluid experiences much higher turbulence intensity when compared to the particles. This could be because the particles have not had the chance to respond to the fluid's turbulence. However, as the interaction time increases, both the particles and the carrier fluid reach a certain point where they merge and share the same intensity. From Figure 3-2, we also know that increasing the mass content will decrease the intensity of the carrier fluid.

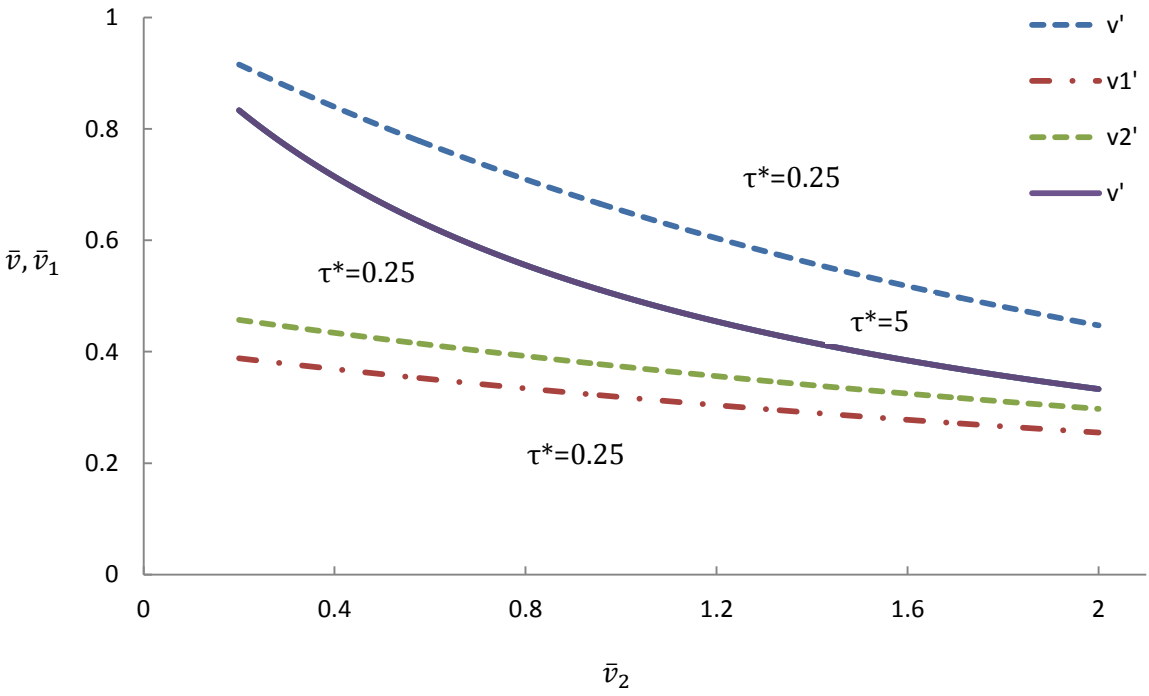

Figure 3-5: Turbulence intensity of large ($\bar{v}_1'$) and small ($\bar{v}_2'$) particles with varying mass contents and interaction ($\gamma 1=\gamma 2=\gamma/2$, $\omega=0.8$, $\tau^*=0.25$ & 5)

The results of the theory put forward by Yarin and Hetsroni [9] have been recreated and outlined in this chapter for two main reasons:

1. To show that at the transitional drag regime, the equation for calculating the particle response time and the momentum equation in which the theory has been derived, results in a more linear behavior (Figure 3.2 & 3.4) for coarse polydisperse particles.
2. To show some of the limitations with this model and why it is not realistic to compare fine particles in a turbulent particle-laden jet.

Chapter 5 will compare Figures 3.2-3.4, which are based on Stokes drag law, with that of the proposed trends using the transitional drag law regime. It will then compare the transitional drag law regime with the numerical results obtained for the square-particle laden jet.

Chapter 4: Numerical Setup and Theory

4.1 GOVERNING EQUATIONS

FLUENT (ANSYS, Inc.) uses the finite volume method to discretize the governing equations for the continuous and discrete phase. This section will discuss the continuity and momentum equations that are used for the discrete phase and the continuous phase and explain how the standard k-ε turbulence model is calculated in FLUENT (ANSYS, Inc.).

4.1.1 Conservation of Mass

The continuity equations for both phases are described below:

$$\frac{\delta \rho_p}{\delta t} + \nabla . \left(\rho_p \overrightarrow{v_i}\right) = 0 \tag{4.1}$$

$$\frac{\delta \rho}{\delta t} + \nabla . (\rho \vec{v}) = 0 \tag{4.2}$$

where ρ_p is the density of the particle, ρ is the density of the fluid, v_i and v is the particle velocity (index i refers to the particle size; 1 for large and 2 for small) and fluid velocity respectively. This is the conservation form of the continuity equation which is derived based on an infinitesimal element that is fixed in space [62]. The first terms of Equation 4.1 and 4.2 represent the time rate of mass increase for the discrete and continuous phase respectively [62]. The second terms of each equation represent the net mass flow out of the control volume [62].

4.1.2 Continuous Phase

The equation of motion for the continuous phase is outlined below:

$$\frac{\delta}{\delta t}(\rho \vec{v}) + \nabla . (\rho \vec{v} \vec{v}) = \nabla \mathrm{p} + \nabla . \tau_s + \rho \vec{g} + \vec{F} \tag{4.3}$$

Equation 4.3 is the Navier Stokes equation for viscous flow. The first term on the left-hand side represents the time rate at which the net momentum increases. The second term represents the convective flux of the momentum [63]. On the right-hand side, terms such as static pressure, P, the stress tensor, τ_s, and the gravitational and external body forces are included. The only body force included in this study is the gravitational force.

4.1.3 Discrete Phase

For the Lagrangian reference frame the equation of motion for a single particle is defined as:

$$\frac{dv_p}{dt} = F_D(v - v_i) + \frac{g(\rho_p - \rho)}{\rho_p} + F_X \tag{4.4}$$

where F_D is the drag force and F_x is an additional acceleration term. The Saffman's lift force is not included because the particles are relatively large. The thermophoretic force is not used because the flow is considered isothermal. The gravitational force is turned on and applied in the y- direction. The drag and drag coefficient are calculated using the following equations:

$$F_D = \frac{18\mu}{\rho_p d_p^2}\left(\frac{C_D Re_p}{24}\right) \tag{4.5}$$

$$C_D = a_1 + \frac{a_2}{Re_p} + \frac{a_3}{Re_p^2} \tag{4.6}$$

where a_1, a_2, and a_3 vary depending on the particle Reynolds number and settling velocity of each particle. This equation was developed by Morsi and Alexander [64] and is applicable for transitional and Newton's drag regimes. This equation does not vary much in the values

calculated from the Schiller and Naumann [65] transitional drag law equation. The differences in values vary by 0.33%. The particle Reynolds number is defined as:

$$Re_p = \frac{\rho d_p |v_p - v|}{\mu} \tag{4.7}$$

where v_p is the velocity of the particle and v is the velocity of the continuous phase. The net velocity between the discrete and the continuous phase is the slip velocity. In the discrete random walk (DRW) stochastic model, V is defined as:

$$V_i = \bar{v}'_i + v' \tag{4.8}$$

which includes the mean fluctuating velocity component and the fluctuating velocity to the continuous phase.

For flows with two-way coupling, the momentum exchange between the continuous and discrete phase is defined below:

$$F = \sum \left(\frac{18\mu C_D Re_p}{24\rho_p d_p^2} (v_p - v) + F_{other} \right) \dot{m}_p \Delta t \tag{4.9}$$

This allows the momentum of a particle to change as it travels through the control volume [66].

4.1.4 Standard k-ε Turbulence Model

The transport equations for the standard k-ε turbulence model are defined as:

$$\frac{\delta}{\delta t}(\rho k) + \frac{\delta}{\delta x_j}(\rho k u_j) = \frac{\delta}{\delta x_j}\left[\left(\mu + \frac{\mu_t}{\sigma_k} \right) \frac{\delta k}{\delta x_j} \right] + G_k + G_b - \rho\varepsilon - Y_M + S_K \tag{4.10}$$

and

$$\frac{\delta}{\delta t}(\rho\varepsilon) + \frac{\delta}{\delta x_j}(\rho\varepsilon u_j) = \frac{\delta}{\delta x_j}\left[\left(\mu + \frac{\mu_t}{\sigma_\varepsilon}\right)\frac{\delta\varepsilon}{\delta x_j}\right] + C_{1\varepsilon}\frac{\varepsilon}{k}(G_k + C_{3\varepsilon}G_b) - \frac{C_{2\epsilon}\rho\varepsilon^2}{k} + S_\varepsilon \qquad (4.11)$$

where S_k and S_e are user-defined terms, G_k and G_b are the turbulent kinetic energy from the mean velocity gradient and the buoyancy respectively, Y_m is the fluctuating dilatation, $C_{1\varepsilon}$, $C_{2\varepsilon}$ and $C_{3\varepsilon}$ are constants [67].

4.2 Problem Setup and Geometry

The particle-laden jet under study is displayed in Figure 4-1. This geometry consists of a 0.2x0.2x0.2 m^3 box with an inlet and outlet on opposite faces. The inlet has a hydraulic diameter of 0.04 m. The inlet and outlet each have an area of 0.0016 m^2. The inlet and the outlet are aligned along the center plane about the z-axis. The coordinates of the center point of the inlet and outlet are (0, 0.17, 0.1) and (0.2, 0.03, 0.1) respectively. This geometry is fixed in space and time i.e., there are no moving walls. Air and bidisperse particles enter the inlet at specified velocities and turbulence intensities.

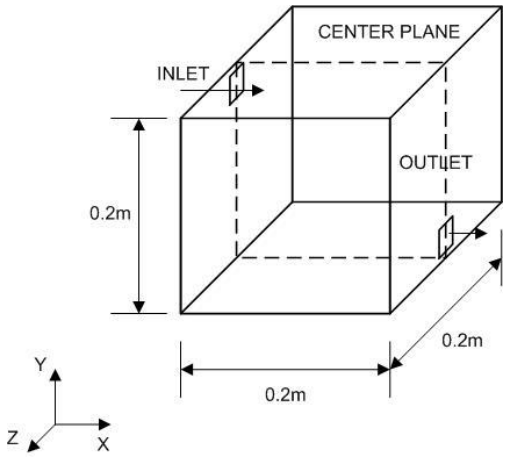

Figure 4-1: Model setup of the geometry

4.2.1 Mesh Setup

The geometry was created in ANSYS Design Modeler and then meshed in ICEM CFD. Because this geometry is composed of squares, the Cartesian grid in ICEM CFD was chosen to mesh the entire geometry. Figure 4-2 displays the pre-mesh setup of the Cartesian grid. See the appendix for instructions on how this mesh was developed in ICEM CFD. The final grid selected was 40x40x40 (see the Grid independence section) which is composed of 64,000 cells (0.005m for each cell) with an aspect ratio of 1.732. The aspect ratio indicates how much a cell has stretched [68]. For a unit cube, the maximum distance is 0.866 and the minimum distance is 0.5 so this results in an aspect ratio of 1.732 [68]. This maximum distance is obtained using Pythagorean's Theorem for a cube. If it were not a perfect cube, this number would deviate from 1.732. See Appendix B for more information on the calculation of the aspect ratio. The maximum cell squish resulted in a value of zero for this mesh. The cell squish indicates the quality of the cells. A value near one is indicated as poor mesh quality for unit cubes, and the closer to zero the better the meshing quality [68].

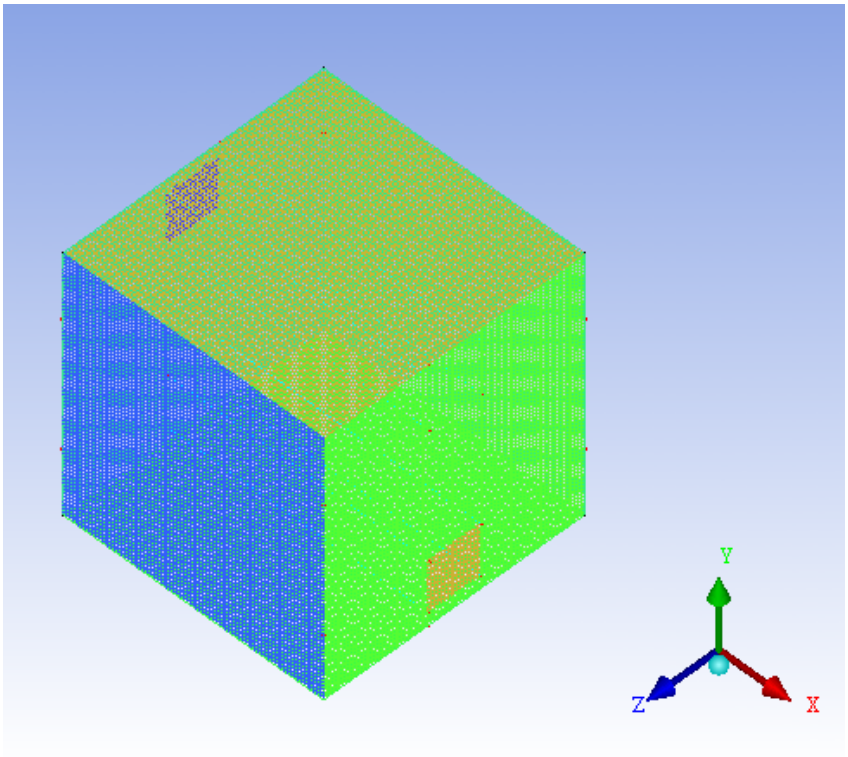

Figure 4-2: Premesh setup of 40x40x40 geometry in ICEM CFD

4.2.2 Boundary Conditions

Once the mesh was generated, it was then imported into FLUENT (ANSYS, Inc.) Setup. The boundary conditions for the geometry are summarized in Table 4-1 below. The default for the wall boundary conditions in FLUENT (ANSYS, Inc.) were applied to each of the walls. This means that the no-slip condition was applied to each of the walls. No-slip condition ensures that when the air hits the wall, the velocity will be set to zero. Each of the walls were set to reflect. This ensures that when the particles collide with the walls, they will bounce off the surfaces. This is based on the default coefficient of restitution value of 1 used in FLUENT (ANSYS, Inc.). This coefficient indicates how much momentum is retained after a particle hits a wall [69]. Small particles, around 1 micron tend to have rebound energies too low to overcome the adhesion force on the walls [15]. These particles are usually set to trap, but the particles under

this study are set to reflect due to their size. The size of the particles vary between 775-1000 microns. The boundary condition of the floor was set to trap. The reason for this was to ensure that the particles would not exit the control volume (which are one of Yarin and Hetroni's [9] assumptions). The inlet was set to the velocity inlet boundary condition. The velocity specification method in FLUENT (ANSYS, Inc.) was set to components, and a specified x-velocity was entered. The specification method for the turbulence was set to a pre-determined turbulence intensity and hydraulic diameter. For more information on the turbulence intensity, see Chapter 5. The outlet was set to the pressure outlet boundary condition. The pressure was set to standard air and temperature conditions, which resulted in the default zero-gauge pressure. The backflow specification method was set to "components", and the direction was set to 1. This is used in the event of the flow reversing direction, and this value also indicates in which direction it should travel [70]. Like the inlet conditions, the turbulence specification method was set to "turbulence intensity and hydraulic diameter" for the outlet vent and the turbulence intensity for the outlet was set to 0%. This is because there are no particles exiting the domain so the intensity at the outlet is negligible.

Table 4-1: Boundary Conditions

Inlet	Velocity Inlet
Outlet	Outlet Vent
Left wall	Wall
Right Wall	Wall
Floor	Trap
Ceiling	Wall
Back Wall (minus outlet)	Wall
Front Wall (minus inlet)	Wall

4.2.3 Computational Setup

This section describes the parameters chosen for each simulation in FLUENT (ANSYS, INC.).

In each of the simulations, flow is steady, incompressible and the gravity function is turned on and set to -9.81 m/s^2 in the y-direction. Turning on gravity indicates that the particles are in a domain where there is gravity, and thus cannot float or move without the use of the continuous fluid. If this function is not turned on, unrealistic results will be produced. Figure 4-3 shows a case for the particle dispersion of the turbulent kinetic energy in the square jet with and without the mesh.

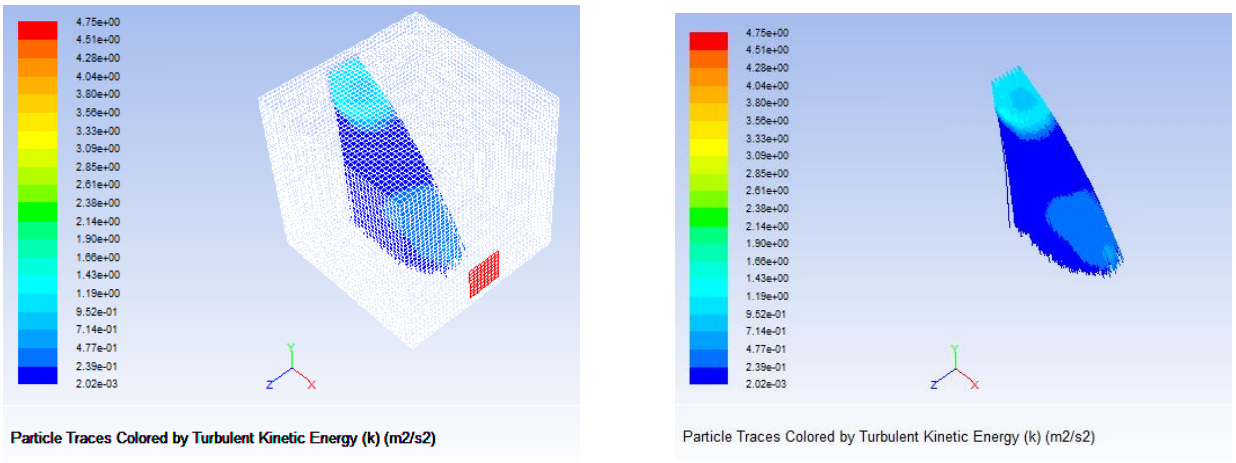

Figure 4-3: Particle dispersion for the turbulent kinetic energy in the square jet with mesh (left) without mesh (right)

The turbulence model used is the standard k-ε model with the standard wall function selected. This model had a faster convergence rate and accuracy for this flow condition than the RNG turbulence model. Near-wall treatment is very important in particle dispersion [71]. ANSYS uses a log-law model for the standard wall functions. They are valid for fully-developed turbulent flows and boundary layers that are in equilibrium [67]. As long as $30 < y^+ < 300$, the log-law wall function will be applied in the simulation [67]. y+ can be defined as:

$$y^+ = \frac{\rho U^* y}{\mu} \tag{4.12}$$

where u* is the frictional velocity closest to the wall and y is the distance closest to the wall. Table 4-2 shows the values computed for y^+ for each of the varying mass loading ratios considered for this study (in the cases in which the mass loading ratios are equal). These values are calculated based on the final mesh selection of 40x40x40 which is 0.005m for each cell. Limits outside the log-law layer will provide inaccurate results inside the laminar viscous sublayer, and will not consider low Reynolds number effects [67]. If y^+ is lower than 11.2 then the enhanced wall function is recommended [67].

Table 4-2: Summary of wall conditions

$\gamma_1 = \gamma_2$	Velocity (m/s)	Boundary layer length (m)	y+
0.125	3.75	0.04	90
0.25	7.5	0.04	105
0.375	12.5	0.04	120

The discrete phase (Lagrangian) model is enabled, and interacts with the continuous phase. The drag law is set to spherical because the particles are coarse and spherical, and the particles are not in the Stokes drag regime. The particle Reynolds number is much greater than one. For more information on the drag law refer to section 2.2.3.2. The maximum number of time steps is set to 20,000. This is not the same as the unsteady time steps for a transient simulation. This value tells the limit at which to calculate the trajectory of a single particle [66]. A very high number of times steps results in more computation time, but yields better predictions on the trajectory of a particle. The default value in FLUENT (ANSYS, Inc.) is 500.

The particles are classified as inert and the density of each particle size is different. Chapter 5 outlines the variations of the densities based on each particle size. Each density is entered in the materials section. The discrete random walk (DRW) approach is used, and the number of tries is set to 48 for this mesh-type, which will model 3,072 particles for each particle size. The DRW is a stochastic model that includes the effects of Gaussian distributed random velocity fluctuations in the flow field [66]. Using this approach allows random effects to occur

as the particles are dispersed in the domain [66]. Because the volume fraction of the particles was roughly 10^{-4} for each of the mass contents, two-way turbulence coupling was enabled.

In the Solution Methods, the pressure-velocity coupling is set to SIMPLE. To ensure that mass is conserved, the SIMPLE algorithm uses the pressure and velocity relationship [72]. The spatial discretization is set to Least Squares Based, Second Order, Second Order Upwind, Second Order Upwind, and Second Order Upwind for the Gradient, Pressure, Momentum, Turbulent Kinetic Energy, and Turbulent Dissipation Rate respectively. The second order upwind scheme uses a multidimensional linear approach to approximate the Taylor series expansion at the cell center of each cell. This scheme is not recommend for flows with discontinuous pressure gradients [72].

The under-relaxation parameters control how the variables are updated in each iteration [72]. The relaxation parameters were not altered for any of the simulations and were left at the default values in FLUENT (ANSYS, INC.). The residuals converged between 10^{-16} to 10^{-7} for each simulation. The iterations ran until the residuals no longer changed with the increase in iterations. There were minor fluctuations in the residuals but they remained relatively constant after thousands of iterations. At that point, it was assumed that the solution converged to a steady state solution.

4.3 Grid Independence Study

The purpose of a grid independence study is to ensure that the numerical solution is independent of the grid chosen. One way to ensure this is to run multiple grids with different sizes to verify the accuracy of the solution, and also to see whether the solution changes with the size of the grid. Normally in a grid independence study, one would continue to double the grid until there is a point where there is no change in the solution from the previous grid. This grid independence study will consider three grid sizes 20x20x20, 40x40x40, and 80x80x80 (ICEM CFD, the meshing software, was not able to double the geometry beyond 80x80x80 for this particular geometry). Table 4-3 displays a summary of the mesh size, cells, and the approximated time each grid size completed a simulation.

Table 4-3: Mesh size information used for the grid independence study

Mesh Size	Cells	Δx	Estimated CPU Time (hours)
20x20x20	8000	0.01	0.5
40x40x40	64,000	0.005	1.5
80x80x80	512,000	0.0025	15

One of the biggest errors that occur in numerical simulations is the discretization error. The discretization error is the error that comes from the algebraic representation of the partial differential equations in a discrete domain [73]. The discretization error can be reduced with the use of a grid independence study. Figure 4-4 shows the x-velocity profile of the three grid sizes

chosen which are distributed along the center z-plane at x=0.01m. Observing this figure, one can see that there is not much difference in each of the solutions obtained but looking at Table 4-3 there is a drastic difference in the computation time required for the 80x80x80 grid. Because the 40x40x40 grid does not require significant computational time and has slightly better accuracy than the 20x20x20 grid, the 40x40x40 grid was selected and will be used in this study.

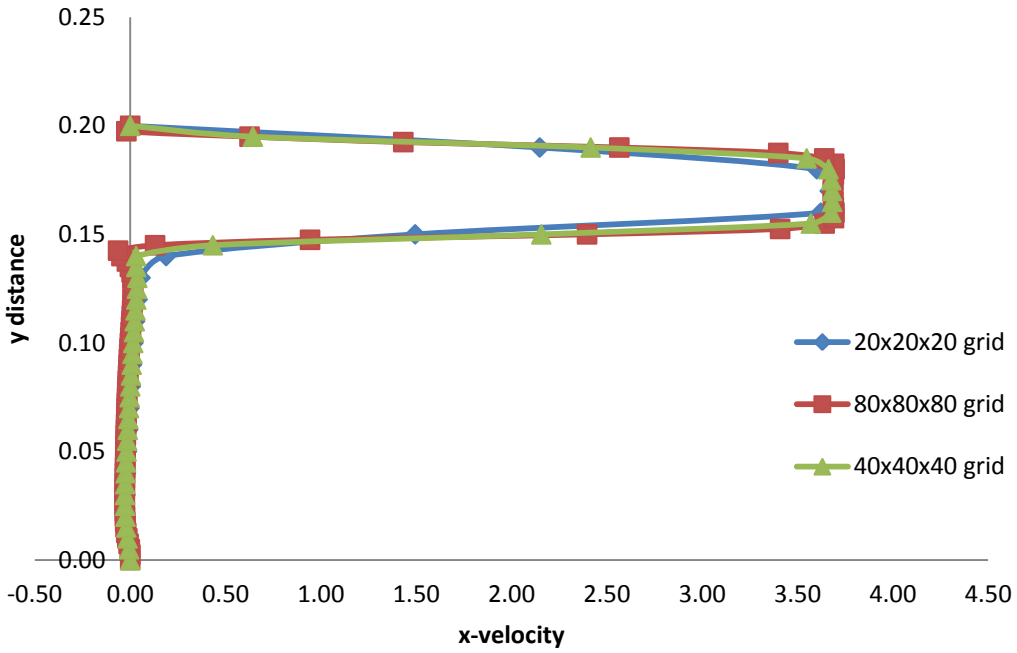

Figure 4-4: X-velocity profile for varying grids

Chapter 5: Turbulence Modulation: Numerical Investigation

This chapter compares the work done by Yarin and Hetsroni with the CFD results of a square particle-laden jet. It also compares these CFD results with the new analytical model developed for the transitional drag regime.

5.1 Limitations with Yarin and Hetrsoni et al. [9] Model

When Yarin and Hetsroni [9] developed the analytical model for turbulence intensity for polydisperse particles, it was derived based solely on Stokes' drag law. In order to utilize Stokes' drag law, the particle Reynolds number must be less than one. Based on the equations that are derived, this would amount to very fine particles and would result in at least billions of particles to be analyzed for the geometry outlined in Chapter 4 (larger geometries result in much more particles). To show how this would result in a large amount of particles, let us consider the case where the mass loading ratio, γ = 0.25 and the particle ratio, ω=0.8. In order to be in Stokes drag:

$$\omega = \frac{d2^2}{d_1^2} = \frac{\left(8.94x10^{-6}\right)^2}{(10^{-5})^2} \cong 0.8 \tag{5.1}$$

$$M_{p1} = \rho_p \dot{V}_p = (762)\left[\frac{4}{3}\pi\left(\frac{10^{-5}}{2}\right)^3\right] = 3.99x10^{-13}kg \tag{5.2}$$

$$N = \frac{M\gamma_1}{M_p} = \frac{9.8x10^{-3}kg(0.125)}{3.99x10^{-13}kg} = 3{,}072{,}000{,}000\ particles! \tag{5.3}$$

the particles must be very small as shown in Equation 5.1. In the cases where $\gamma 1=\gamma 2$, the mass of the particles are equal. The density at each particle size varies. The density also varies with the number of particles. In order to have realistic particle densities, the number of particles must increase. So, if one wanted to use 3,072 particles in the domain for this particular case, the

density of the large and small particles would result in $7.6x10^8$ kg/m^3 and 10.6 $x10^8$ kg/m^3 respectively. This is not realistic or computationally efficient for a single computer. One would need a super computer to run such simulations. In order to have realistic densities and computation times, larger particles must be considered. Larger particles result in a change of the drag regime due to a larger particle Reynolds number, and the effects of wakes. In order to consider larger particles, Yarin and Hetrsoni's [9] model must be modified to account for particles that fall in the transitional drag regime.

5.2 Residence Time and Steady State Simulations

Figure 5-1 displays a similar relationship from Figure 3-1, but instead represents the relationship between the residence time and the turbulence intensity of the air, with large and small particles. The residence time is the time a particle spends in a control volume [74]. It is calculated as follows:

$$\tau = \frac{\dot{V}}{\dot{q}}$$

where $\dot{V}$ is the volume of the control volume, and $\dot{q}$ is the volumetric flow rate of the particles entering into the system. In this particular case, the residence time begins when the particles enter the system and it ends when they hit the floor. At the final residence time, all particles are on the floor. At this time, the particles become trapped, and can travel no further. In observing Figure 5-1, there appears to be a trend different from that of Figure 3-1. In Figure 3-1, the particles begin with a low turbulence intensity. As time increases the particles mix with the air and eventually they both reach a time in which their respective turbulence intensities are equal.

In Figure 5-1, the particles and air initially begin with the same turbulence intensity. As residence time increases, however, the air and particles begin to increase and decrease

respectively. Also, it appears as if the residence time is causing the turbulence intensity to change, but what is actually occurring is a change in the turbulence intensity as it moves through the control volume, not as a function of time. This change in turbulence intensity is a function of the trajectory and location of the particles. This simulation is a steady-state simulation which means that the properties of the flow do not change with time. The properties can, however, change with space.

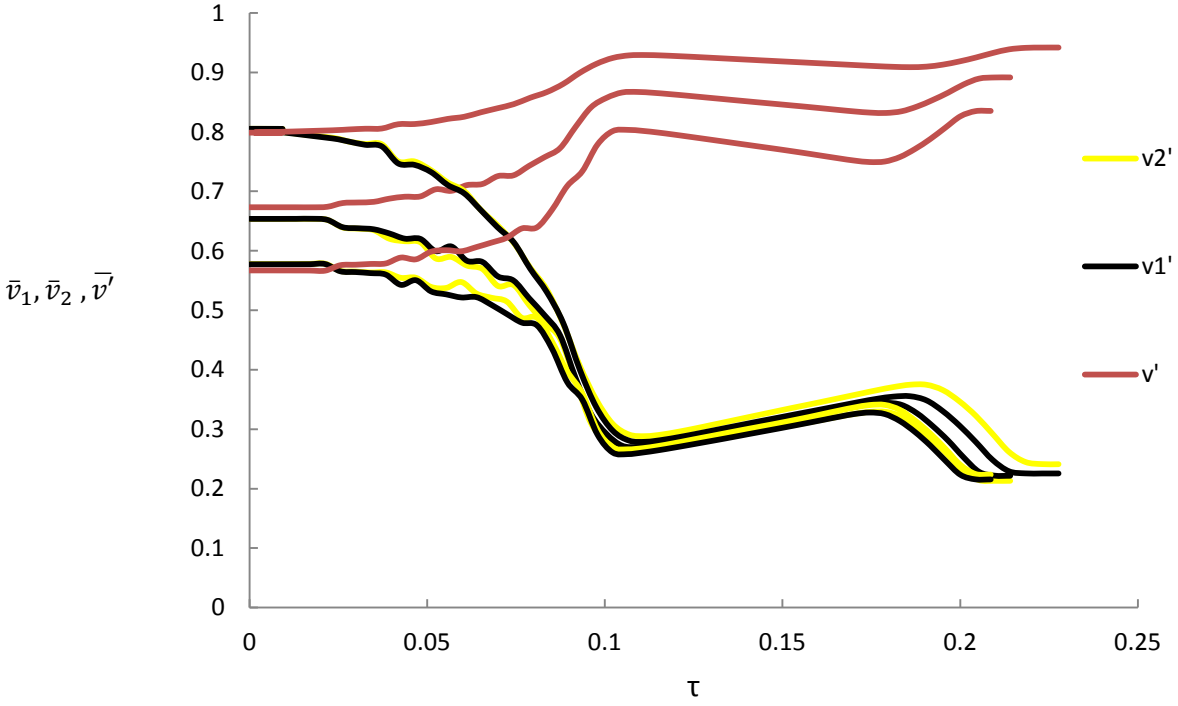

Figure 5-1: Turbulence intensity of large, small particles, and air as a function of residence time at γ=0.25, 0.5, and 0.75 (Standard k-ε results)

The difference in these trends (Figure 3-1 and Figure 5-1) lie in the boundary conditions outlined for each. In Yarin and Hetsroni's [9] model, the boundary conditions for the particles are zero. This explains why initially, near time=0, the turbulence intensity for the particles is close to zero in Figure 3-1. In the CFD model, the boundary conditions for each particle size is

$\tilde{v}'_i = |v_0{}' - v_s|$. When the flow enters the inlet, the settling velocity of the particle is not reached and is very close to zero. This is why, at the residence time = 0, the particles and air are initially equal to each other. As the particles travel, and thus residence time increases, the settling velocity is eventually reached. Thus, the turbulence intensity of the particles decreases as the air increases in the flow field.

5.3 Proposed Modification for Transitional Drag Regime

Chapter 3 outlined the derivation of the momentum equation, considering the effects of the Stokes drag regime, which was developed by Yarin and Hetsroni [9]. This section proposes a modification, to the equations used in Chapter 3, which will account for the transitional drag regime.

Assuming the transitional drag law developed by Schiller-Naumann [65], $C_D = \frac{24}{Re_i}(1 + 0.15Re_i^{0.687})$ for the particles, equation 3.2 can now be expressed as:

$$\frac{dv_i'}{dt} = \frac{\left(\frac{1}{2}\right)\rho\frac{24}{\tilde{v}_i d_i}v\tilde{v}_i|\tilde{v}_i|(f_i)}{m_i}(1 + 0.15Re_i^{0.687}) = \frac{18\mu\tilde{v}_i}{d_i^2\rho_i}(1 + 0.15Re_i^{0.687}) \tag{5.4}$$

$$\tau = \frac{18\mu}{d_i^2\rho_i} \tag{5.5}$$

For simplicity we will set the term $\tilde{v}_i(1 + 0.15Re^{0.687})$ to some constant C. The additional term, $\tilde{v}_i$, is included in the C term because we have a new initial condition.

Combining equations 3.1 and 3.5, representative of a mixture with two particle sizes, i.e., bidisperse, the new equations results in:

$$\frac{d\bar{v}_1'}{dt} = \tau_1^{-1} C_1[1 - (1+\gamma_1)\bar{v}_1' - \gamma_2 \bar{v}_2'] \tag{5.6}$$

$$\frac{d\bar{v}_2'}{dt} = \tau_2^{-1} C_2[1 - \gamma_1 \bar{v}_1' - (1+\gamma_2)\bar{v}_2'] \tag{5.7}$$

Equations 5.6 and 5.7 are then divided to eliminate the time term.

$$\frac{d\bar{v}_2'}{d\bar{v}_1'} = \frac{\tau_2}{\tau_1}(C_1/C_2)[1 - \gamma_1 \bar{v}_1' - (1+\gamma_2)\bar{v}_2'] \tag{5.8}$$

The density, the viscosity and the constant in the relaxation time, τ, are cancelled and the only terms left are the diameters of each particle size, i.e., $\omega = \frac{\tau_2}{\tau_1} = \frac{d_2^2}{d_1^2}$. The C_1 and C_2 terms next to ω, we will name it omega multiplier, i.e., ω*. This term accounts for the additional terms needed for the transitional drag regime. Everywhere there is an ω term in the previous analytical model, this new term will be multiplied by it to account for the effects of the transitional drag regime. This parameter changes the curves from Figure 3-1 to a linear relationship.

One important item to note, in Yarin and Hetsroni's model [9], the initial conditions were set at $\tilde{v}_i = 0$. This will not be the case for this regime. The particle fluctuational velocity will be the relative velocities of the carrier fluid and particles, i.e., $\tilde{v}_p = v_0' - v_p'^{(i)}$. The initial condition was changed because a solution does not exist when $\tilde{v}_p = 0$ for this drag regime. Yarin and Hetsroni [75] showed this in part 3 of their research. The omega multiplier will vary for each case because the settling velocity changes with each particle density, i.e. mass loading ratio.

Figure 5-2 shows a graph comparing Yarin and Hetsroni's [9] model with coarse particles for the case where γ=0.25. In this case the Re_{p1}=222 and Re_{p2}=256. The black solid and dashed lines represent the results from Yarin and Hetsroni's [9] model. The purple and green markers represents the CFD results obtained using FLUENT (ANSYS, Inc.). Observing this figure, one

can see that Yarin and Hetsroni [9] model has more of a curve at the tip. This is due to the particles following the fluid fluctuations closely, where-as the black curve is very linear. The dashed black curve is due to the Stokes drag regime and the particles having a very low Stokes number (St << 1). The purple and green markers represent the air and the small and large particles and are in the transitional drag regime and the Stokes number is very high.

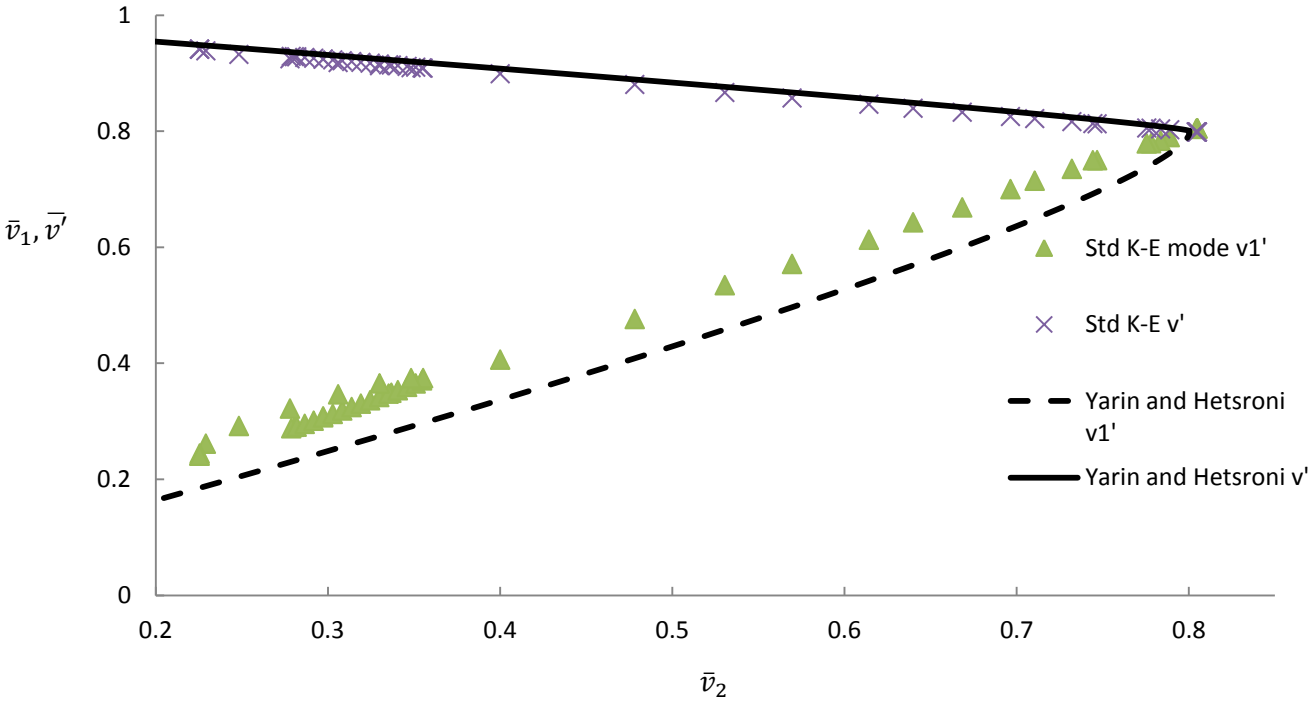

Figure 5-2: Comparison of Yarin and Hetrsoni's [9] analytical model with the CFD model for the case where γ=0.25 and Rep=215

In Figure 5-3, the new analytical model and the results from the Standard k-ε model are shown. It is observed that both the CFD and new analytical model closely, and linearly, resemble each other. This is due to particles being in the same drag regime as the new analytical model. The results section will now consider comparisons between the new model and the CFD results.

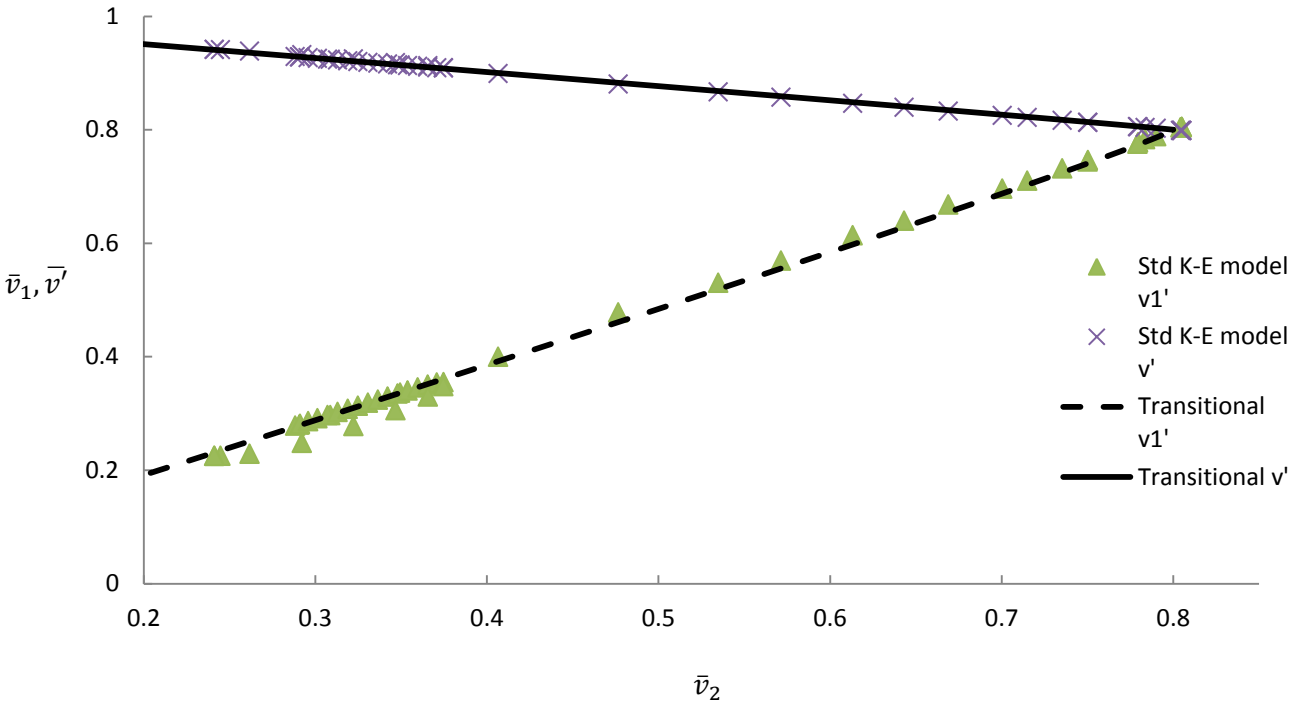

Figure 5-3: Comparison of the new analytical model with the CFD model for the case where γ=0.25 and Rep=215

5.3.1 Further Explanation about the Omega Multiplier

As stated earlier, the omega multiplier, ω*, is a term, when multiplied by the old analytical model, accounts for the effects in the transitional turbulence regime. It is dependent on the density and settling velocity of each of the particles, and will vary for each particle loading ratio. It must be computed accurately to correctly acquire the behavior of the turbulence modulation of the carrier fluid and particles. This section will explain how the values are obtained.

$$\omega^* = \frac{C_1}{C_2} = \frac{\tilde{v}_2(1+0.15Re_1^{0.687})}{\tilde{v}_1(1+0.15Re_2^{0.687})} \tag{5.9}$$

where

$$\tilde{v}'_i = |v'_0 - v_s| \tag{5.10}$$

Equation 5.9 is the calculation for the omega multiplier. To obtain the particle fluctuating velocity, $\tilde{v}_i$, one must utilize the initial air fluctuating velocity, $\bar{v}'_o$, and settling velocity of the particle, v_s. This initial condition is valid because of the assumption that the flow is already fully-developed, and the particles have reached their settling velocity shortly after time=zero. The particle interaction time must be larger than one, or the omega multiplier will result in incorrect values. It should be noted that because this coefficient has not been tested on a wide range of particle-laden jets, it is not standardized. With further testing, it could be standardized and thus applied to a wide range of flows in the transitional region. It should also be noted that this parameter is valid only for the assumptions outlined in Chapter 3 of Yarin and Hetsroni's [9] model. When the particles are in the Stokes regime, the omega multiplier is equal to 1.

5.3.2 Limitations with Omega Multiplier

As with all analytical models, there are limitations within this proposed model. One of the limitations is that the model works accurately if $\gamma_1=\gamma_2$ i.e., the masses of each particle size are equal. If these terms are not equal, the analytical model will not predict the results from the CFD results. This value only seems to be applicable over the range 1.1-1.35 in the studies tested thus far. The discussion on Figure 5-4 will explain why this parameter only works for cases in which $\gamma_1=\gamma_2$.

5.4 RESULTS AND DISCUSSION

Since it has been shown that the new analytical model has good agreement with CFD, this section will only consider the results and discussion obtained from the analytical and numerical results developed by the author.

Table 5-1 summarizes the values applied to Figures 5-4 to 5-6. It displays varying mass content values and shows how the the ω* varies along with other parameter such as turbulence intensity and Reynolds numbers. The initial turbulent kinetic energy of the air was held constant at 1.215 for Table 5-1. The initial velocity at the inlet and the turbulence intensity percentage entered into FLUENT (ANSYS, Inc) resulted in the initial turbulent kinetic energy value of 1.215. This consistency helps to show how the turbulence intensity and particles interact with each other. Because this value was made constant, the particle interaction time for each of the particles decreased with increasing mass content. The initial velocity of the continuous fluid increased with increasing mass content because the settling velocity varies due to density variations for each of the particles. These velocities were chosen so that the relative velocity between the particles and the carrier fluid can be very close to negligible. This table also shows that the omega multiplier is inversely proportional to the mass content.

Table 5-1: Summary of parameters

γ_1	γ_2	γ	V_0	ω	ω^*	τ^*	Re_{p1}	Re_{p2}	Re	Turbulent Intensity (%)
0.125	0.125	0.25	3.6735	0.8	1.191	176.91	222	256	10,061	24.5
0.25	0.25	0.5	4.39	0.8	1.156	88.45	343	393	12,024	19.69652
0.375	0.375	0.75	5.2	0.8	1.147	58.97	440	505	14,243	17.3077
0.5	0.5	1	6	0.6	1.352	28.73	525	718	16,434	15
0.5	0.5	1	6	1	1	61.81	525	525	16,434	15
0.2	0.8	1	6	0.8	1.766	27.64	298	802	16,434	15
0.66	0.34	1	6	0.8	0.943	65.04	623	476	16,434	15

5.4.1 Turbulence Modulation Results

Once each simulation was calculated in FLUENT (ANSYS, INC.), the particle history data was extracted, arranged, and sorted using macros in Microsoft Excel (see appendix for the Macros). From the results in FLUENT (ANSYS, INC.), the fluctuating velocity of the particles were extracted. They were calculated using the following equation:

$$v'_{iavg} = \sqrt{2k} \tag{5.11}$$

$$\bar{v}_{i,avg} = \frac{v'_{iavg}}{U_m} \tag{5.12}$$

$$V_m = \frac{V_0}{2} \tag{5.13}$$

where $\bar{v}_{i,avg}$ is the average fluctuating velocity for each particle size (large and small), V_m is the mean velocity of the continuous fluid, and k is the turbulent kinetic energy of the particles. The particles were averaged for each particle size. Figures 5-4 to 5-6 represent an average of the turbulent intensity of 3,072 particles for each particle diameter.

Figure 5-4 shows a plot of the turbulence intensity of the fluid against the large and small particles using the new analytical solution. It also displays the results obtained from the Standard k-ε model. One can see that the large particles and the fluid are inversely proportional to the turbulence intensity of the carrier fluid. This is due to the momentum transfer between the carrier fluid and the large particles. As the small particles increase, the turbulence intensity of the large particles decreases. This plot also shows that the numerical results of the CFD simulation coincide with the new analytical model.

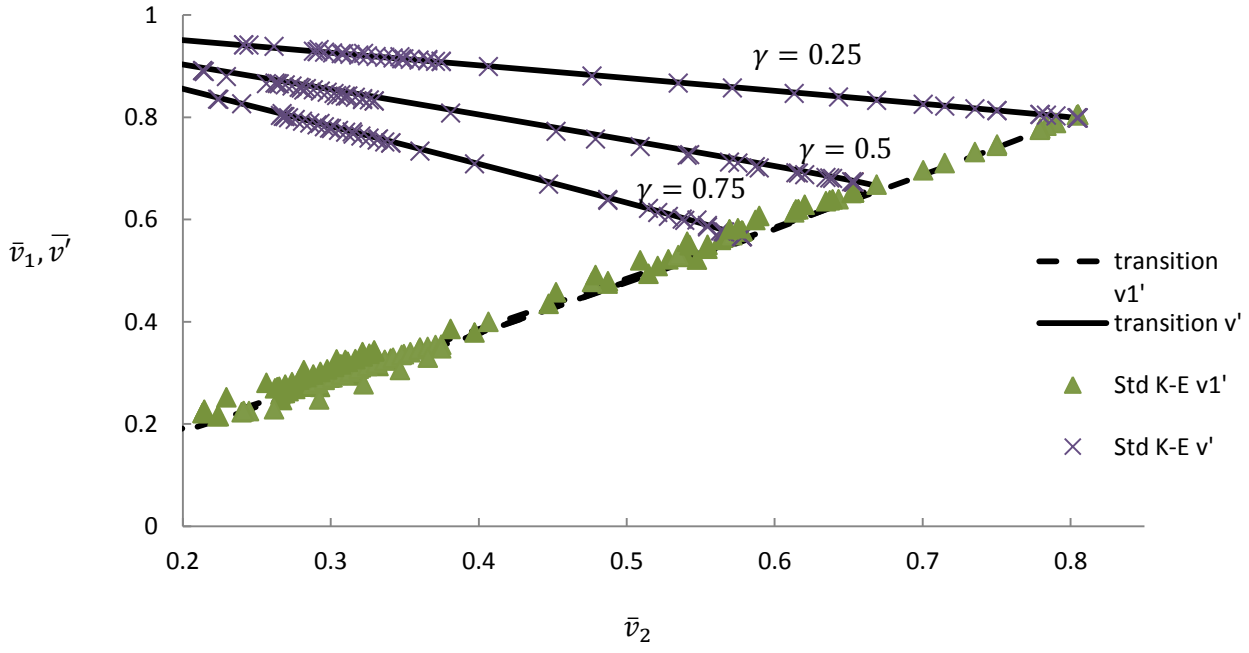

Figure 5-4: Comparison of CFD with analytical model for the turbulent intensity of small and large particles

Figure 5-5 shows the relationship of the turbulence intensity with varying particle-loading ratios. While the mass loading ratios were equal in Figure 5-4, in this figure they are not. The omega multiplier is 1.766 and 0.943 for this figure for the cases where m_c=0.25 and m_c=2, respectively. In this figure, m_c=0.25 and 2 which means that the mass contents for the large and small particles are not equal and γ_1=0.2, γ_2=0.8 and γ_1=0.66, γ_2=0.34, respectively. One can see that the modified analytical model does not agree with the numerical simulation for the case where m_c=0.25. This occurrence is due to the large difference in settling velocity. The difference in the settling velocity is 7 m/s for this case. This drastic difference in particle size will cause the particles to collide with each other, and thus behave similarly to four-way coupling. This is because the analytical model does not show good agreement when the mass content ratios are not equal. Based on the volume fraction, the particles are classified as exhibiting the effects of two-way coupling. Due to the difference in velocity, four-way coupling could be exhibited due to particle-particle collision between the large and small particles. The analytical model is only applicable when the particles are considered dilute, which would mean either one-way or two-way coupling. Because the particles are behaving similar to four-way coupling (in the m_c=0.25 case), the model does not predict the CFD results. The CFD models show a trend that is similar to Figure 3-5 except that it is linear, which incorporates the transitional drag regime. The CFD models for the cases in which the mass contents are not equal cannot be compared with the new analytical model due to the limitations of this model.

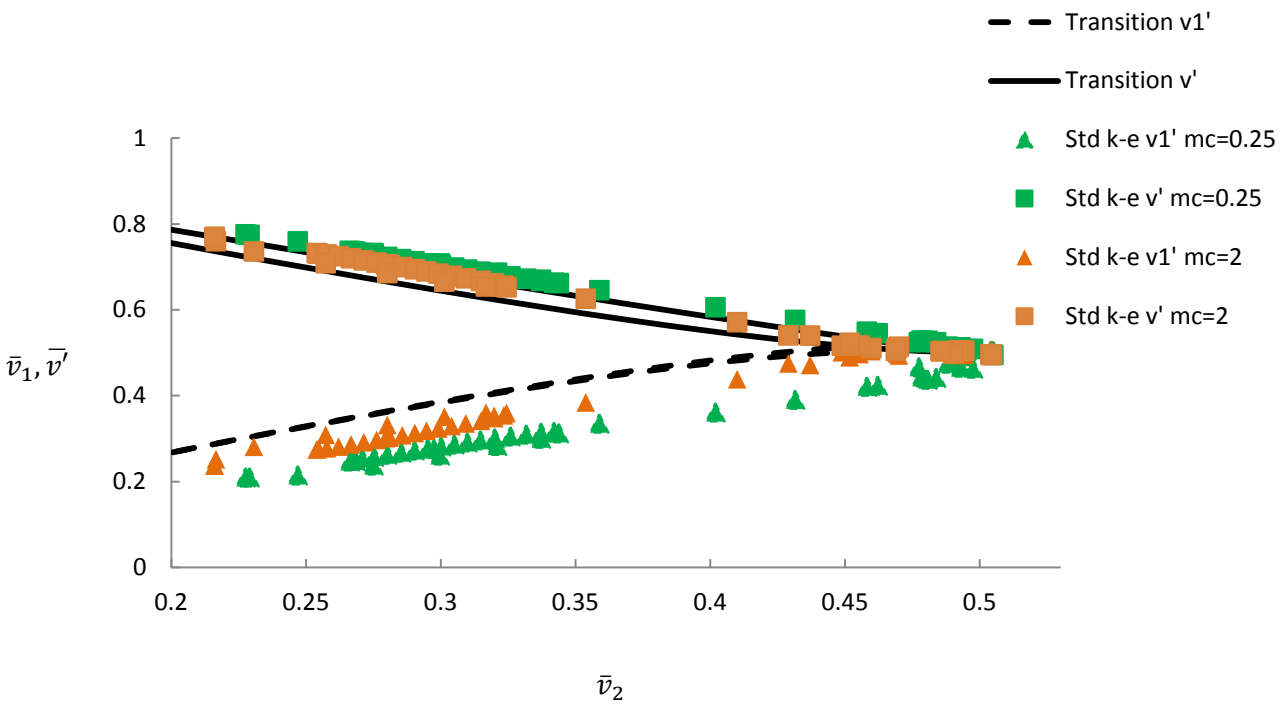

Figure 5-5: Turbulence intensity of unequal mass contents (γ=1, ω=0.8)

Figure 5-6 shows the relationship between the effects of varying particle-loading ratios and turbulence modulation. This graph is interesting because one can see the importance of the monodisperse assumption. Often-times, when particles are modeled, it is assumed that the flow is monodisperse. In the Yarin and Hetsroni [9] model, there is a wider gap in the difference between turbulence intensity for various particle loading ratios. If one is measuring turbulence intensity in the transitional regime, then using the monodisperse assumption can be used without producing large error. As the particle loading ratio increases, the turbulence intensity increases for smaller particles, as well as larger particles. The difference in turbulence intensity between the cases of ω=0.6 and ω=1 are not noticeable, and the conclusion is that for the transitional regime, monodisperse can be applied without significant accuracy. In the region observed, the trend is linear, but it looks similar to Figure 5-2 when it is expanded outward.

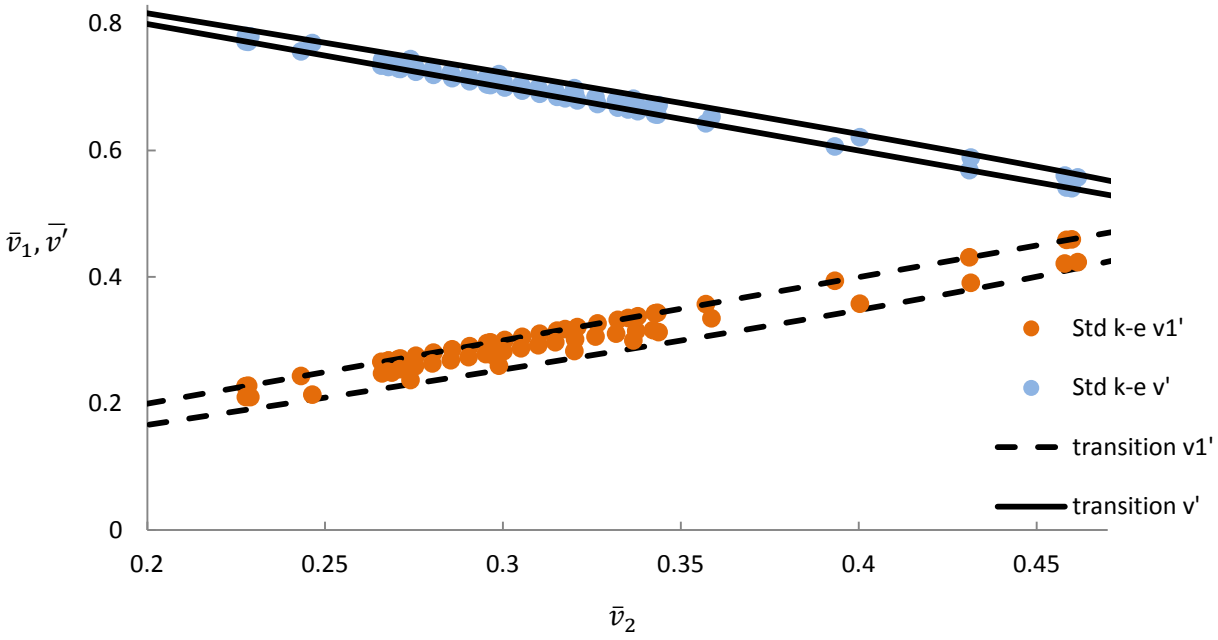

Figure 5-6: Effects of turbulence intensity with varying particle diameter ratios

5.4.2 Concentration Distribution Results

Figure 5-7 shows the variation of the concentration distribution along the y-axis for varying mass content values. Studies in indoor particle dispersion often utilize concentration to measure how particles are dispersed in an enclosed space. Often times, the monodisperse assumption is applied and the author wants to investigate the effects of the monodisperse assumption for concentration distribution. The concentration distribution pattern shown in Figure 5-7 is a similar trend to those of previous studies [28]. The concentration was calculated using the Particle in Source Cell method. This numerical code was developed by Dr. Qingyan Chen at Purdue University and is used with permission. This code is imported into FLUENT (ANSYS, INC.) as a User Defined Function (UDF) and obtains concentration that has been accumulated for the discrete phase method [76]. The values are stored in a user-defined memory

(UDM) location. One can see from each of the plots in Figure 5-7 that the concentration is largest at the inlet for each of the mass content values. In Figure 5-7a, each of the mass content values are similar for the concentration, and are dispersed uniformly. In Figure 5-7b, the smallest mass content value, γ=0.25, has a slightly larger concentration at x=0.04m; this could be because the particles are travelling much faster and are less dense, thus have a higher entrainment. At x=0.1m, the overall concentration decreases for each of the mass content values. Another noticeable trend here is that the larger mass content values γ=0.5 and γ=0.75 were close in concentration at each region investigated.

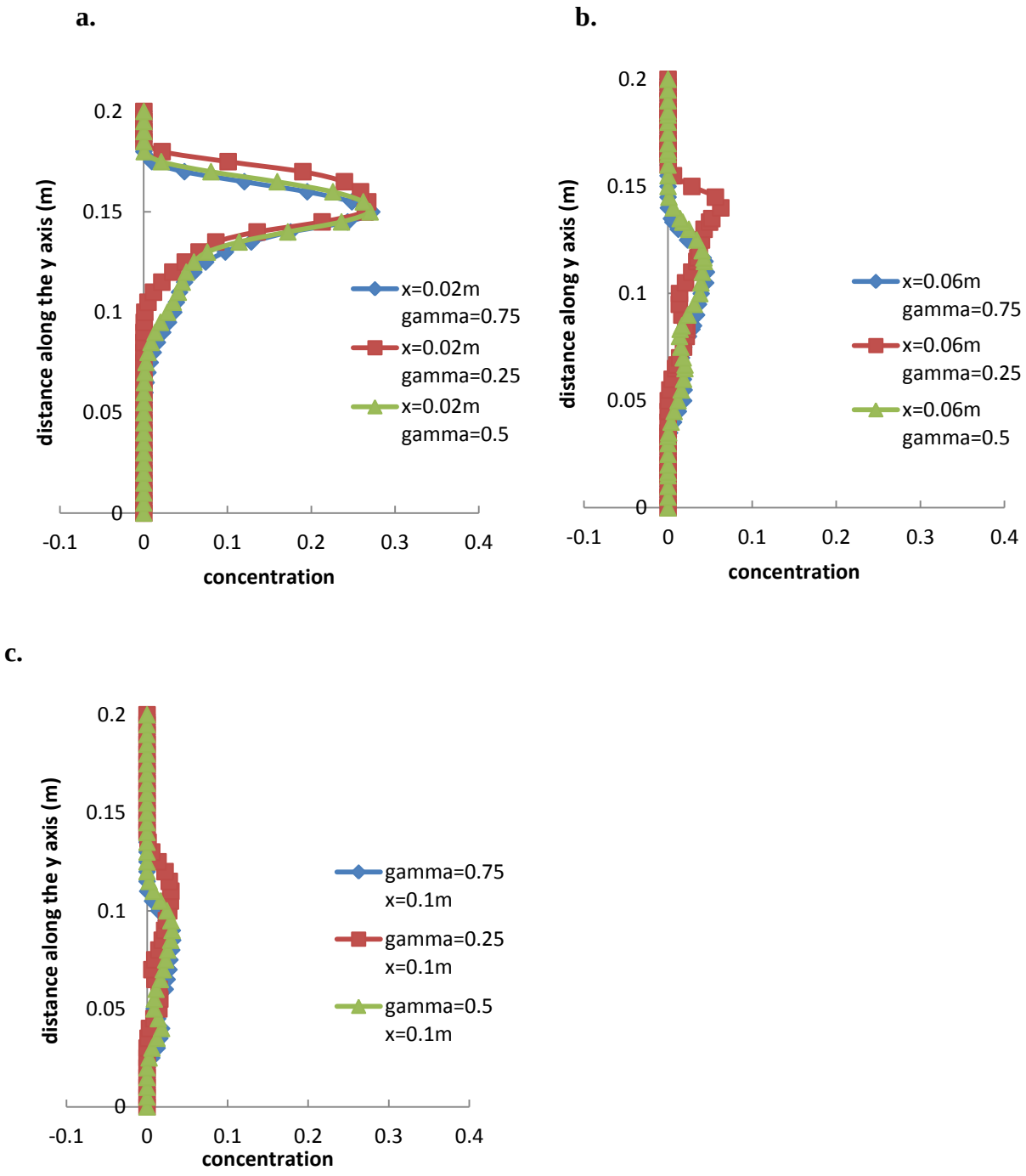

Figure 5-7: Concentration distribution along the y-axis: a) at x=0.02m b) x=0.06m c) x=0.1m

Figure 5-8 shows the concentration distribution for varying particle size ratios. The blue curves represent the monodisperse distributions and the red is bidisperse. At x=0.06m and x=0.1m, both particle ratios are relatively similar in concentration. However at x=0.02m, the bidisperse profile has a lower concentration distribution than the monodisperse one. This means that when monodispersed is assumed for concentration distribution, it is slightly over-predicted and could result in higher than normal values for the concentration.

a.

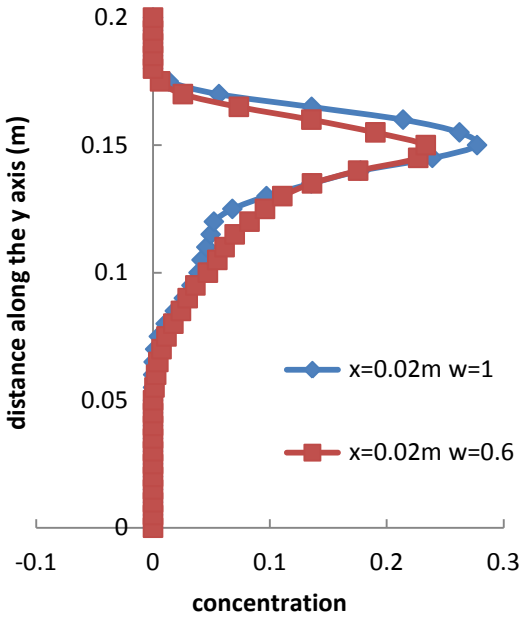

b.

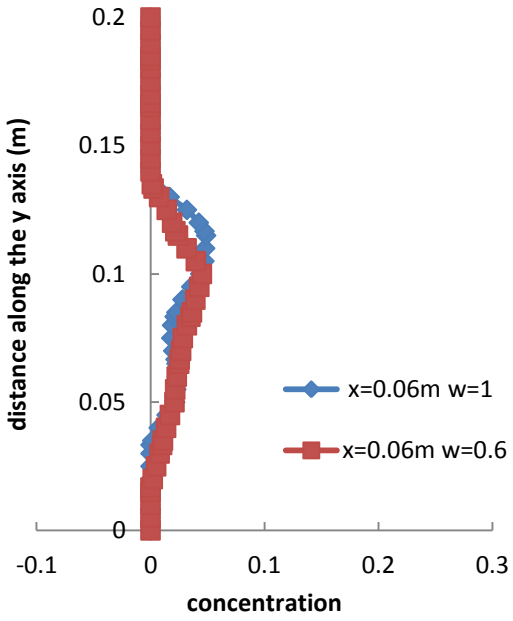

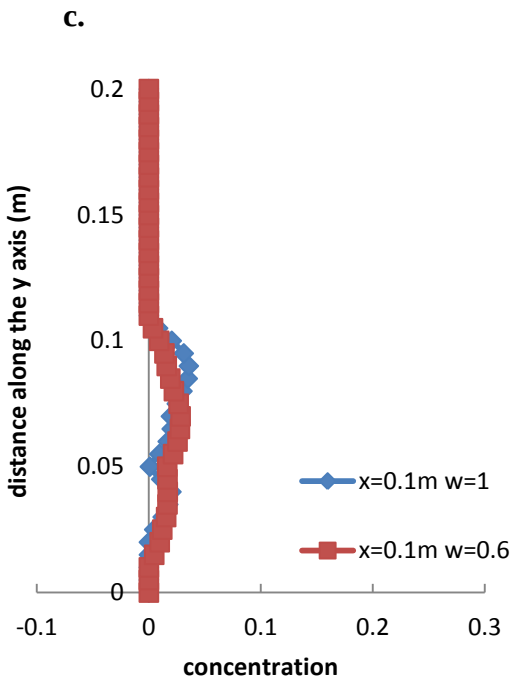

Figure 5-8: Concentration distribution of varying particle size ratios along the y-axis: a) x=0.02m, b) x=0.06m, c) x=0.1m

Figures 5-9 and 5-10 shows the contour and vector plots of the x-velocity and the turbulent kinetic energy, for the case where γ=0.25. Observing Figure 5-10, the turbulent kinetic energy and the x-velocity is highest at the outlet. This may be due to the stagnation pressure that is created near the outlet and as a result a buildup of turbulent kinetic energy and x-velocity. This can be seen from the vector plots in Figure 5-9 and 5-10. The initial input of the turbulence intensity in the boundary conditions helps calculate the turbulent kinetic energy and the particle interaction time. The turbulent kinetic energy dissipates as it moves further away from the jet but increases as it gets closer to the outlet. This is due to a decrease in momentum as a result from carrier fluid and particles interacting with each other. Similar trends are noticed with the other mass content and particle ratios. The other contour plots are available in Appendix D and E.

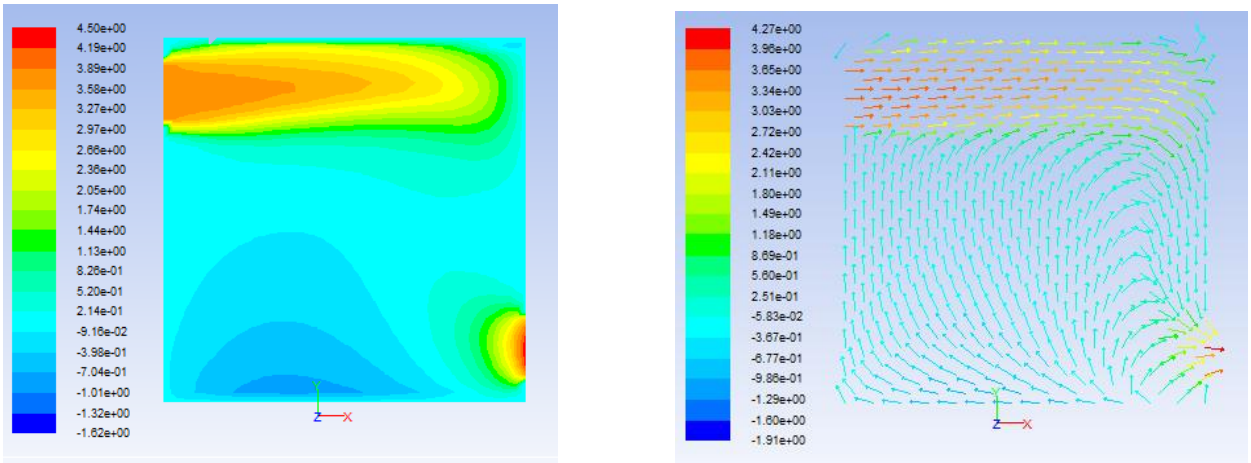

Figure 5-9: Contour plot of x-velocity (left) and Vector plot of x-velocity (right) at the center plane of the box

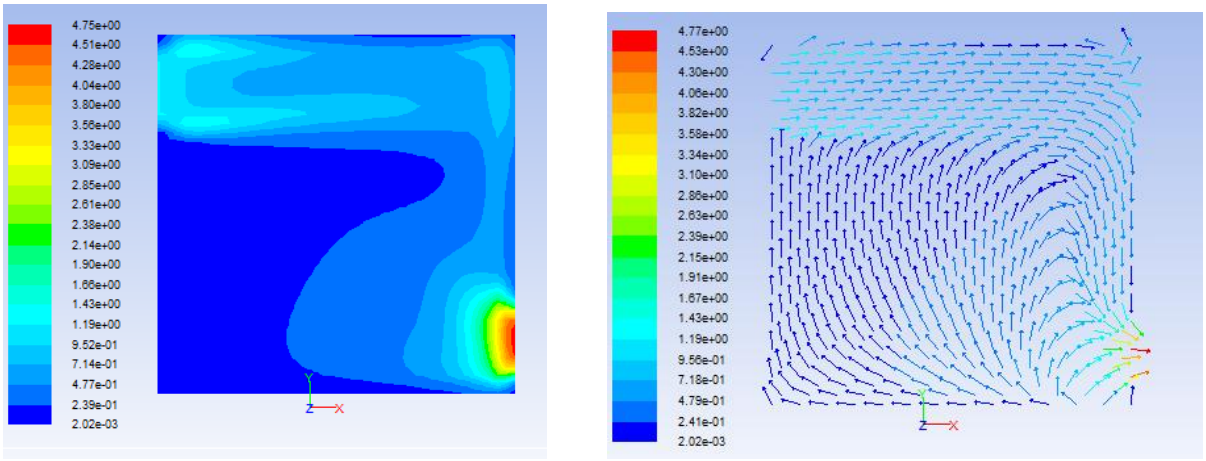

Figure 5-10: Contour plot of turbulent kinetic energy (left) and vector plot of turbulent kinetic energy (right) at the center plane of the box

Chapter 6: Conclusions and Future Work

This study investigated the effects of turbulence modulation of bidispersed particles in a square turbulent jet. In the first chapter a set of objectives were outlined to be completed. The results of the objectives are summarized as follows:

1. The CFD agrees with the modified analytical results, which accounts for the transitional regime. For the cases where $\gamma_1 \neq \gamma_2$, the CFD results exhibit a linear trend that could result in greater accuracy, should four-way coupling be considered. Because the model is applicable only to dilute flows, the CFD results need to be compared with analytical data that incorporates four-way coupling.
2. An analytical model was developed and modified to account for the transitional regime and showed good results with the CFD results, except in the case where the mass contents are not equal i.e. ($\gamma_1 >> \gamma_2$). This is due to the model being applied to the dilute regime only. The effects of turbulence intensity for monodisperse and bidisperse particles showed that when analyzing turbulence intensity in the transitional regime, the monodisperse assumption would not sacrifice accuracy.
3. The effects of concentration distribution for varying mass content and particle ratios showed that the monodisperse assumption slightly overly predicts the concentration in certain regions of the flow field. The larger mass contents i.e., γ, exhibited similar patterns in the concentration distribution. Assuming monodisperse in this regime would not sacrifice great accuracy for the concentration distribution.

Although Yarin and Hetsroni's [9] model showed sound trends for turbulence intensity for small and large particles, it does not seem feasible to duplicate the model experimentally or numerically. In the future, it would be worth considering the development of an analytical

model that will incorporate the effects when $\gamma_1 \neq \gamma_2$. Testing the range of the transitional analytical regime is another item to consider. It would be interesting to observe this when applied to other jet configurations. Making this model apply to a wide range of flows can be a large step in understanding turbulence intensity and particle dispersion. A sure method for successful application of this model is through experimental testing. This would require tools such as Laser Doppler Anemometry or Particle Image Velocimetry to measure the fluctuating velocity components.

At the start of this thesis, the motivation outlined the relevance of this research and how critical it is that particle dispersion is understood. The aim of this thesis is to help provide more knowledge to, and understanding of, particle dispersion. This can help reduce fossil-fuel emissions, increase understanding of dispersion patterns in agents used for biological terrorism, and improve HVAC systems indoor air quality by extension.

Bibliography

1. *Health Aspects of Chemical and Biological Weapons*, 1970: Geneva, Switzerland: World Health Organization.
2. Lai, A., Thatcher, T.,, *Inhalation Transfer Factors for Air Pollution Health Risk Assessment.* Air and Waste Management Association, 2000. **50**: p. 1688-1699.
3. Cole, E.C., Cooke, C.E.,, *Characterization of infectious aerosols in health care facilities: an aid to effective engineering controls and preventive strategies.* American Journal of Infection Control, 1998. **26**: p. 453-464.
4. *An Introduction to Indoor Air Quality*.
5. Solomon, S., Qin, D., Manning, M., Chen, Z., Marquis, M., Averyt, K. B., Tignor, M., Miller, H.L., *Contribution of Working Group I to the Fourth Assessment Report of the Intergovernmental Panel on Climate Change, 2007* 2007: Cambridge, United Kingdom and New York, NY USA.
6. Climate, B.o.A.S.a., *America's Climate Choices*, 2011, The National Academies Press: Washington, DC.
7. Laboratory, A.N. *Fuel Injection and Spray Research*. July 2011.
8. Mandø, M., et al., *Turbulence modulation in dilute particle-laden flow.* International Journal of Heat and Fluid Flow, 2009. **30**(2): p. 331-338.
9. Yarin, L.P., Hetsroni, G., *Turbulence Intensity in Dilute Two-Phase Flows - 1: Effect of Particle-Size Distribution on the Turbulence of the Carrier Fluid.* International Journal of Multiphase Flow, 1994. **20**(1): p. 1-15.
10. Gore, R.A., Crowe, C. T., *Effect of Particle Size on Modulating Turbulent Intensity.* International Journal of Multiphase Flow, 1988. **15**(2): p. 279-285.
11. Elghobashi, S., *On Predicting Particle-Laden Turbulent Flows: direct simulation and closure models.* Applied Scientific Research, 1991. **48**: p. 301-314.
12. Varaksin, A., *Turbulent Particle-Laden Gas Flows*. Atomic, Optical and Plasma Physics2007, New York: Springer.
13. Loth, E., *Computational Fluid Dynamics of Bubbles, Drops and Particles*2013: Cambridge University Press.
14. Okuyama, K., Yuu, S., , *Powder Technology: Fundamentals of Particles, Powder Beds, and Particle Generation*, 2006. p. 103-113.
15. Hinds, W., *Aerosol Technology: Properties, Behavior, and Measurement of Airborne Particles*. 2nd ed1999, New York: 2nd Ed. John Wiley and Sons Inc.
16. *Drag Coefficient*, Wikipedia The Free Encyclopedia: http://en.wikipedia.org/wiki/Drag_coefficient.
17. Clift, R., J. R. Grace, and M. E. Weber, , *Bubbles, Drops, and Particles*1978, New York: Academic Press.
18. Ahmadi, G. *Particle Transport, Deposition and Removal II*. 2002.
19. Zhang, J., Li, A., , *Study on particle deposition in vertical square ventilation duct flows by different models.* Energy Conversion and Management, 2008. **49**: p. 1008-1018.
20. Tian, Z.F., Tu, J.Y., Yeoh, G.H., Yuen, R.K.K., , *Numerical studies of indoor airflow and particle dispersion by large eddy simulation.* Building and Environment, 2007. **42**: p. 3483-3492.
21. Tian, L., Ahmadi, G., , *Particle deposition in turbulent duct flows-comparisons of different model predictions.* Journal of Aerosol Science, 2007. **38**(4): p. 377-397.
22. Chen, Q., Zhang, Z,. *Comparison of the Eulerian and Lagrangian methods for predicting particle transport in enclosed spaces.* Atmospheric Environment, 2007. **41**: p. 5236-5248.
23. Lai, A., Chen, F., , *Modeling particle deposition and distribution in a chamber with a two-equation Reynods-averaged Navier-Stokes model.* Journal of Aerosol Science, 2006. **37**: p. 1770-1780.

24. Lai, A.C.K. and F. Chen, *Modeling particle deposition and distribution in a chamber with a two-equation Reynolds-averaged Navier–Stokes model.* Journal of Aerosol Science, 2006. **37**(12): p. 1770-1780.
25. Chen, F., Yu, Simon C. M., Lai, Alvin C. K.,, *Modeling particle distribution and deposition in indoor environments with a new drift–flux model.* Atmospheric Environment, 2006. **40**(2): p. 357-367.
26. Beghein, C., Jiang, Y., Chen, Q., , *Using Large Eddy Simulation to Study Particle Motions in a Room.* Indoor Air, 2005. **15**: p. 281-290.
27. Gao, N.P. and J.L. Niu, *Modeling particle dispersion and deposition in indoor environments.* Atmospheric Environment, 2007. **41**(18): p. 3862-3876.
28. Zhao, B., Caiqing, Y., Yang, X., Liu, S., , *Particle dispersion and deposition in ventilated rooms: Testing and evaluation of different Eulerian and Lagrangian models.* Building and Environment, 2008. **43**: p. 388-397.
29. Lain, S., Garcia, J.A,, *Study of four-way coupling on turbulent particle laden flows.* Chemical Engineering Science, 2006. **61**: p. 6775-6785.
30. Crowe, C., *Multiphase Flow Handbook*2006, Boca Raton, FL: CRC Press.
31. Mostafa, A.A., Mongia, H. C., McDonell, V. G., Samuelsen, G. S., *An experimental and numerical study of particle-laden coaxial jet flows.* International Journal of Heat and Fluid Flow, 1990. **11**(2): p. 90-97.
32. Mergheni, M.A., Sautet, J.C., Godard, G., Ben Ticha, H., Ben Nasrallah, S., *Experimental investigation of turbulence modulation in particle-laden coaxial jets by Phase Doppler Anemometry.* Experimental Thermal and Fluid Science, 2009. **33**: p. 517-526.
33. Sheen, H.J., Jou, B.H., Lee, Y.T., *Effect of Particle Size on a Two-Phase Turbulent Jet.* Experimental Thermal and Fluid Science, 1994. **8**: p. 315-327.
34. Modarress, D., Tan, H., Elghobashi, S., *Two-Component LDA Measurement in a Two-Phase Turbulent Jet.* AIAA Journal, 1983. **22**(5): p. 624-630.
35. Tsuji, Y., Morikawa, Y., Tanaka, T., Karimine, K., Nishida, S., *Measurement of an Axisymmetric Jet Laden with Coarse Particles.* International Journal of Multiphase Flow, 1988. **14**(5): p. 565-574.
36. Tsuji, Y., Morikawa, Y., *LDV measuremetns of an air-solid two-phase flow in a horizontal piep.* J. Fluid Mech, 1982. **120**: p. 385-409.
37. Wang, B., Zhang, H., Liu, Y. Yan, X., Wang, X., *Particle modulations to turbulence in two-phase round jets.* Acta Mech Sin, 2009. **25**: p. 611-617.
38. Levy, Y., Lockwood, F.C., *Velocity Measurements in a Particle Laden Turbulent Free Jet.* Combustion and Flame, 1981. **40**: p. 333-339.
39. Jou, B.-H., Sheen, Horn-Jiunn., Lee, Yuh-Tyzh., *Particle Mass Loading Effect on a Two-Phase Turbulent Downward Jet Flow.* Part. Part. Syst. Charact., 1993. **10**: p. 173-181.
40. Lee, S.L., Durst, F., *On the motion of particles in turbulent duct flows.* International Journal of Multiphase Flow, 1982: p. 125-146.
41. Devenport, W.J., *Laser Doppler Anemometry*, 2006, Virginia Tech.
42. Mei, C. *Laser Doppler Anemometry*. 2003.
43. Foreman, R., *Mass Loading and Stokes Number Effects in Steady and Unsteady Particle-Laden Jets*, in *Mechanical Engineering*2008, The University of Adelaide.
44. Dynamics, D. *PDA HiDense Spray System*. Available from: http://www.dantecdynamics.com/Default.aspx?ID=712.
45. *Particle Image Velocimetry*, in *Wikipedia, The Free Encyclopedia*.
46. Yuan, Z. and E.E. Michaelides, *Turbulence modulation in particulate flows—A theoretical approach.* International Journal of Multiphase Flow, 1992. **18**(5): p. 779-785.
47. Rizk, M.A. and S.E. Elghobashi, *A two-equation turbulence model for dispersed dilute confined two-phase flows.* International Journal of Multiphase Flow, 1989. **15**(1): p. 119-133.

48. Elghobashi, S., et al., *Prediction of the particle-laden jet with a two-equation turbulence model.* International Journal of Multiphase Flow, 1984. **10**(6): p. 697-710.
49. Tsuji, Y., Morikawa, Y., Shiomi, H., *LDV measurements of an air-solid two phase flow in a vertical pipe.* J. Fluid Mech, 1984. **139**: p. 417-434.
50. Maeda, M., Hishida, K., Furutani, T., *Optical measurements of local gas and particle velocity in an upward flowing dilute gas-solids suspension.* Proc. Polyphase Flow and Transport Technology, 1980: p. 211.
51. Kenning, V.M. and C.T. Crowe, *On the effect of particles on carrier phase turbulence in gas-particle flows.* International Journal of Multiphase Flow, 1997. **23**(2): p. 403-408.
52. Kim, S., K.B. Lee, and C.G. Lee, *Theoretical approach on the turbulence intensity of the carrier fluid in dilute two-phase flows.* International Communications in Heat and Mass Transfer, 2005. **32**(3–4): p. 435-444.
53. Crowe, C.T., *On models for turbulence modulation in fluid-particle flows.* International Journal of Multiphase Flow, 2000. **26**: p. 719-727.
54. *Eulerian Model Theory*, I. ANSYS, Editor 2009.
55. Yan, F., *Numerical Study on Turbulence Modulation in Gas-Particle Flows*, in *Mechanical Engineering*2006, McMaster University.
56. Online, C.W. *RANS-based Turbulence Models*. 2009 [cited 2009 April 2012]; Available from: http://www.cfd-online.com/Wiki/RANS-based_turbulence_models.
57. Shih, T.-H., et al., *A new k-ϵ eddy viscosity model for high reynolds number turbulent flows.* Computers Fluids, 1995. **24**(3): p. 227-238.
58. Ling, W., Chung, J., Crowe, C., *Direct numerical simulation of the two-way coupled interaction between particles and mixing layer.* Proc. R. Soc. Lond., 2000. **456**: p. 2931-2955.
59. Yeoh, G.H., Tu, Jiyuan, *Computational Techniques for Multiphase Flows*2010, Amsterdam: Butterworth-Heinemann.
60. Wang, Q., Squires, K.D.,, *Large eddy simulation of particle-laden turbulent channel flow.* Physics of Fluids., 1996. **8**(5): p. 1207-1223.
61. Almeida, T.G. and F.A. Jaberi, *Large-eddy simulation of a dispersed particle-laden turbulent round jet.* International Journal of Heat and Mass Transfer, 2008. **51**(3–4): p. 683-695.
62. Anderson Jr., J.D., *Computational Fluid Dynamics: The Basics with Applications*. Holman, Jack., Lloyd, John1995, New York: McGraw Hill Inc.
63. Powell, A. *Lectures on Fluid Flow and Kinetics*. Open Courseware MIT, 2003.
64. Morsi, S.A., Alexander, A. J., *An Investigation of Particle Trajectories in Two-Phase Flow Systems.* J. Fluid Mech, 1972. **55**(2): p. 193-208.
65. Schiller, L., Naumanna, A., *Uber die grundelgenden berechnungen bei der schwerkraftaufbereitung.* Zeitung des vereins deutscher ingenieure, 1933: p. 77-318.
66. ANSYS, I., *Discrete Phase (Chapter 15)*, 2009.
67. ANSYS, I., *Turbulence*, in *Theory Guide*2009.
68. ANSYS, I., *Reading and Manipulating Meshes (Chapter 6)*, 2009.
69. ANSYS, I., *Chapter 22: Modeling the Discrete Phase*, in *ANSYS FLUENT 12.0 User's Guide*2009.
70. ANSYS, I., *Task Page Reference Guide (Chapter 33)*, 2009.
71. Kaftori, D., G. Hetsroni, and S. Banerjee, *The effect of particles on wall turbulence.* International Journal of Multiphase Flow, 1998. **24**(3): p. 359-386.
72. ANSYS, I., *Using the Solver (Chapter 26)*, 2009.
73. Slater, J. *Uncertainty and Error in CFD Simulations*. 2008. http://www.grc.nasa.gov/WWW/wind/valid/tutorial/errors.html.
74. Wikipedia, T.F.E. *Residence Time*. http://en.wikipedia.org/wiki/Residence_time.
75. Yarin, L.P., Hetsroni, G., *Turbulence Intensity in Dilute Two-Phase Flows-3 The particles turublence interaction in dilute two-phase flow.* International Journal of Multiphase Flow, 1994. **20**(1): p. 27-44.

76. Zhang, Z. and Q. Chen, *Experimental measurements and numerical simulations of particle transport and distribution in ventilated rooms.* Atmospheric Environment, 2006. **40**(18): p. 3396-3408.

Appendices

A: Instructions on how to mesh Square Particle-Laden Jet in ICEM CFD

1. Open ICEM CFD. Go to File Workbench Readers.
    a. Go to the file path in which the Geometry file is located and click open
    b. Click Apply on the Left task bar (if you labeled your BC's in Design Modeler then click on Create Subset Named Sections before clicking on apply)
    c. You can name your boundary conditions here before going to FLUENT (ANSYS, INC.)
        i. To do so just left click on Parts and click Create Part
            1. You can then select a face or edge to name
2. Click on Solid Simple Display (at the top) and under the Geometry Tree on the left task bar click Surface
3. Go to the Blocking Tab and Create a Block.
    a. Select the entire domain and then click apply.
    b. Go to Split Block and split the block around the areas of the inlet and outlet in both vertical and horizontal directions (There should be square surrounded by the inlet and the outlet. This us to ensure that your inlet and outlet are not included in the block)
4. Go to the Geometry tab and create points.
    a. Enter each of the points located in the figure below.
5. Go back to the Block tab and click on associate.
    a. Associate each of the points with the line that is adjacent and perpendicular to the point so that they are lined up evenly.
6. Go to the Mesh Tab and click on Surface Mesh.
    a. Select the entire geometry and enter the mesh size and height.
    b. For the height just enter the same number as the mesh size. Then click apply.
7. Go back to the Block tab and click on Pre-mesh Params
    a. Select Edge Params
    b. Disable surface so that the edge lines are visible
    c. Click on a line and look in the Edge Params tab to make sure that Uniform is set as the Mesh Law and the correct number of nodes are entered. If not change it there.
    d. Under the blocking tree on the left hand side enable Pre-Mesh and it will ask you to update the mesh. Click yes.
8. Go back to the Mesh tab and click Compute Mesh
    a. Once the mesh is computed, if you named your boundary conditions go to File → Mesh → Load From Blocking
        i. This will ensure that your boundary conditions will be transferred in FLUENT (ANSYS, INC.).
        ii. Make sure that Cartesian is selected.
9. Go to Output Tab
    a. Select solver
        i. On output solver select FLUENT_V6

1. Click Apply

b. Click write input

i. It will ask you to save it in 2D or 3D. 3D should be selected.

1. Click Apply

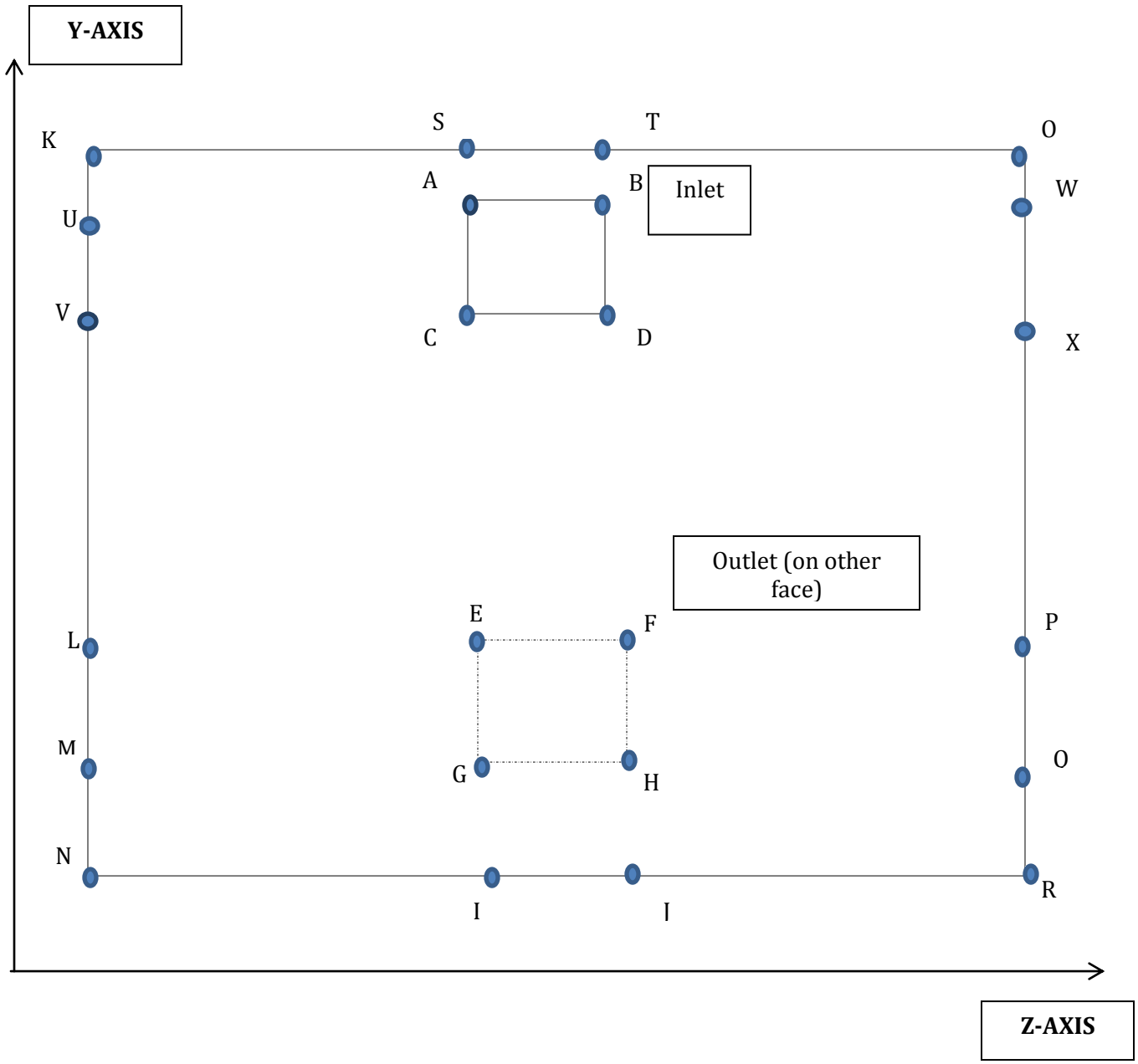

Figure A- 1: Inlet Face for creating mesh in ICEM CFD

Coordinates for Inlet Face

A. (0, 0.19, 0.08)
B. (0, 0.19, 0.12)
C. (0, 0.15, 0.08)
D. (0, 0.15, 0.12)
E. (0, 0.05, 0.08)
F. (0, 0.05, 0.12)
G. (0, 0.01, 0.08)
H. (0, 0.01, 0.12)
I. (0, 0, 0.08)
J. (0, 0, 0.12)
K. (0, 0.2, 0)
L. (0, 0.05, 0)
M. (0, 0.01, 0)
N. (0, 0, 0)
O. (0, 0.2, 0.2)
P. (0, 0.05, 0.2)
Q. (0, 0.01, 0.2)
R. (0, 0, 0.2)
S. (0, 0.2, 0.08)
T. (0, 0.2, 0.12)
U. (0, 0.19, 0)
V. (0, 0.15, 0)
W. (0, 0.19, 0.2)
X. (0, 0.15, 0.2)

The outlet face is similar except the x coordinate will be 0.2 instead of 0.

B: How to Calculate the Aspect Ratio

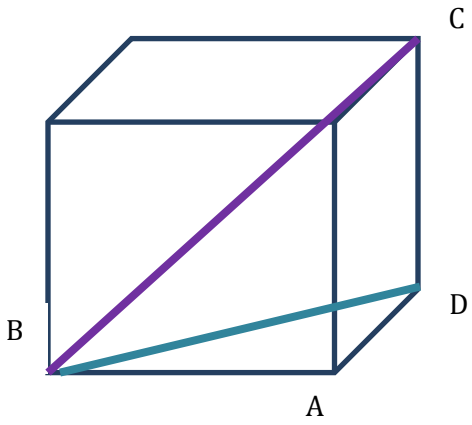

Figure B- 1: Unit Cube for Aspect Ratio Calculation

The aspect ratio indicates how much a cell has stretched. If no stretching occurs then the aspect ratio for a unit cube should be 1.732. Consider the calculation below:

$$Aspect\ Ratio = \ Longest\ Distance\ in\ Cell$$

The longest distance between two nodes are $\overline{BC}$. To find the Longest Distance we use Pythagorean's Theorem:

$$\overline{CD}^2 + \overline{BD}^2 = \overline{BC}^2$$

Since this is a unit cube then $\overline{CD}$ = 1 and $\overline{BD}$ = 1.4142 i.e., $(\overline{AD}^2 + \overline{AB}^2 = 1.4142)$.

$$1^2 + 1.4142^2 = \overline{BC}^2$$

$$\overline{BC} = \sqrt{2.999} = 1.732$$

C: MACROS FOR POST-PROCESSING TURBULENT KINETIC ENERGY DATA

This macro was recorded and ran to organize the turbulent kinetic energy data for 3,072 particles for each particle size into columns separating each particle type (v1' and v2'). Each file would represent a specific residence time depending on how many time steps were included. To save space this is macro is for 1 specific time step. The postprocess files were also recorded macros that organized the data from FLUENT (ANSYS, INC.) into two columns making it easier to calculate the fluctuating velocities (v1' and v2'). Because the recording was so long this process had to be broken into several sub macros. These sub-macros are not included here because it is over 200 pages.

```
Sub AtoZ()
'
' AtoZ Macro
'
Workbooks.OpenText Filename:= _
    "C:\Users\sandyg\Documents\Final Results_files\dp0\FFF\Fluent\New Combined Data\specific.mscl0001" _
    , Origin:=1251, StartRow:=1, DataType:=xlFixedWidth, FieldInfo:=Array( _
    Array(0, 1), Array(12, 1), Array(24, 1), Array(36, 1), Array(48, 1), Array(60, 1)), _
    TrailingMinusNumbers:=True
  Application.Run "macroinfojustincase.xlsm!PostProcess"
  Application.Run "macroinfojustincase.xlsm!PostProcess2"
  Application.Run "macroinfojustincase.xlsm!PostProcess3"
  Application.Run "macroinfojustincase.xlsm!PostProcess4"
  Application.Run "macroinfojustincase.xlsm!PostProcess5"
  Application.Run "macroinfojustincase.xlsm!PostProcess6"
  Application.Run "macroinfojustincase.xlsm!PostProcess7"
   Columns("A:A").Select
  Selection.Cut
  Windows("v2.xlsm").Activate
  Columns("A:A").Select
  ActiveSheet.Paste
  Windows("specific.mscl0001").Activate
```

```
    Columns("B:B").Select
    Selection.Cut
    Windows("v1.xlsm").Activate
    Columns("A:A").Select
    ActiveSheet.Paste
    Windows("specific.mscl0001").Activate
    ActiveWindow.Close
    Windows("v2.xlsm").Activate
End Sub
```

D: CONTOUR PLOTS OF THE X-VELOCITY AND TURBULENT KINETIC ENERGY

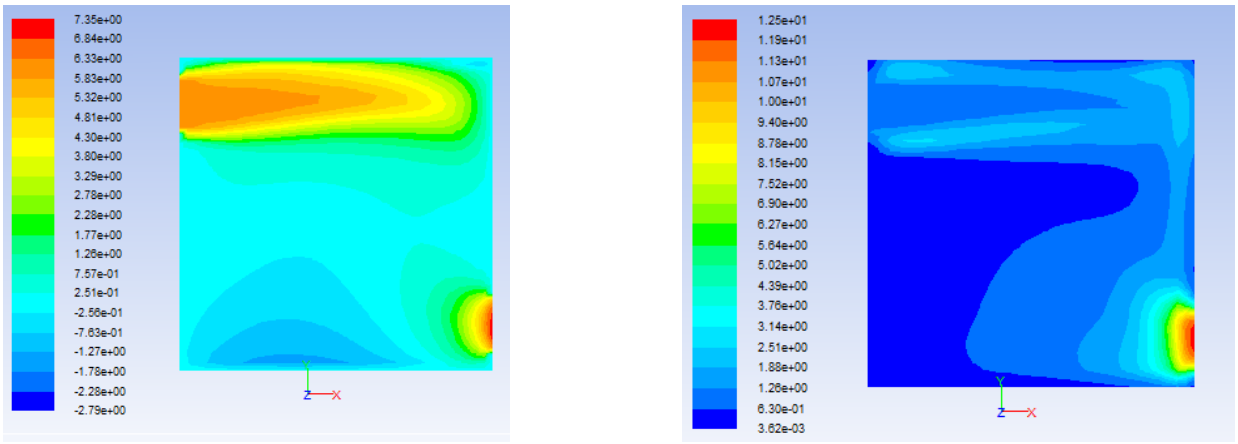

Figure D - 1: X-Velocity (left) and Turbulent Kinetic Energy (right) for w=0.6

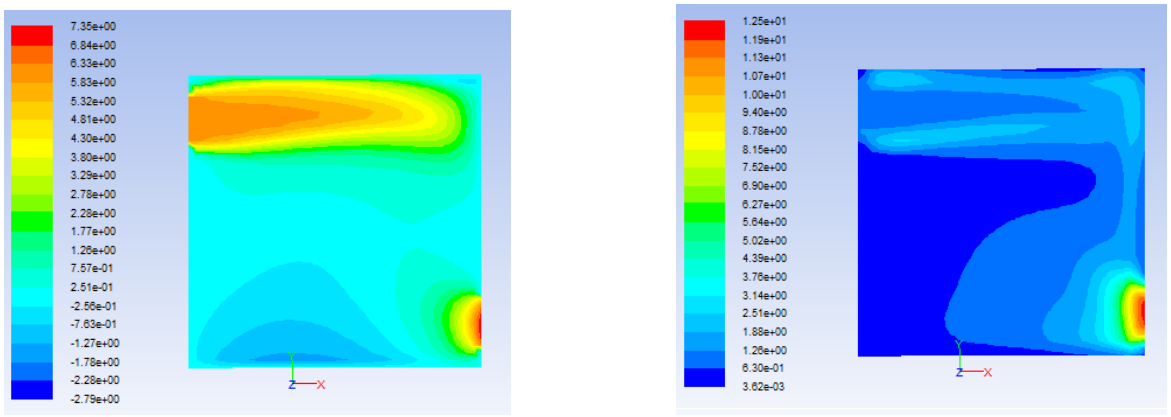

Figure D - 2: X-Velocity (left) and Turbulent Kinetic Energy (right) for w=1

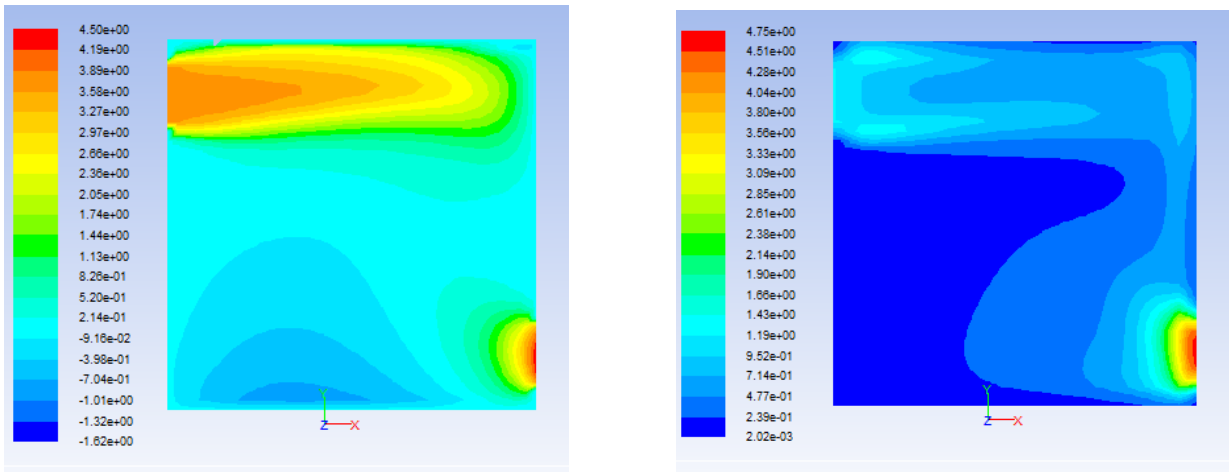

Figure D - 3: X-Velocity (left) and Turbulent Kinetic Energy (right) for γ=0.25

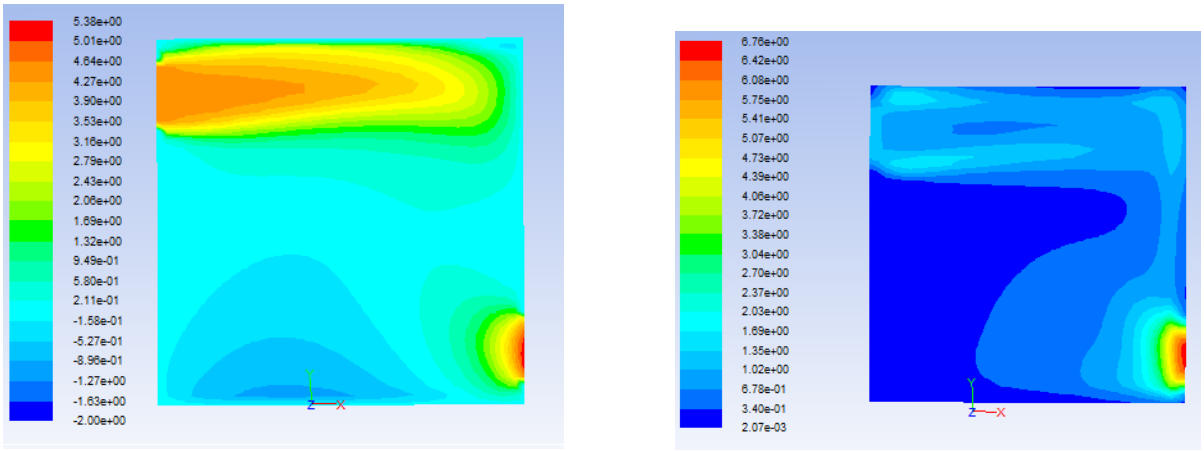

Figure D - 4: X-Velocity (left) and Turbulent Kinetic Energy (right) for γ=0.5

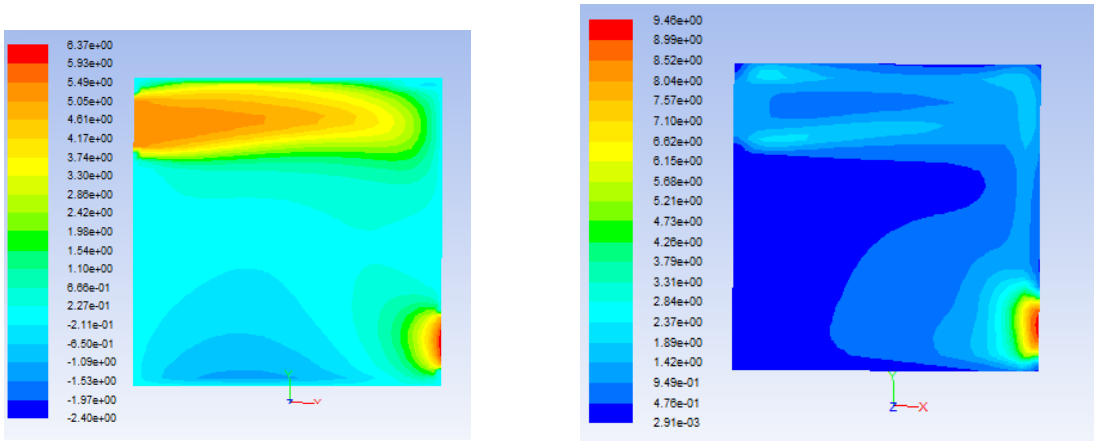

Figure D - 5: X-Velocity (left) and Turbulent Kinetic Energy (right) for γ=0.75

E: VECTOR PLOTS OF THE X-VELOCITY AND TURBULENT KINETIC ENERGY

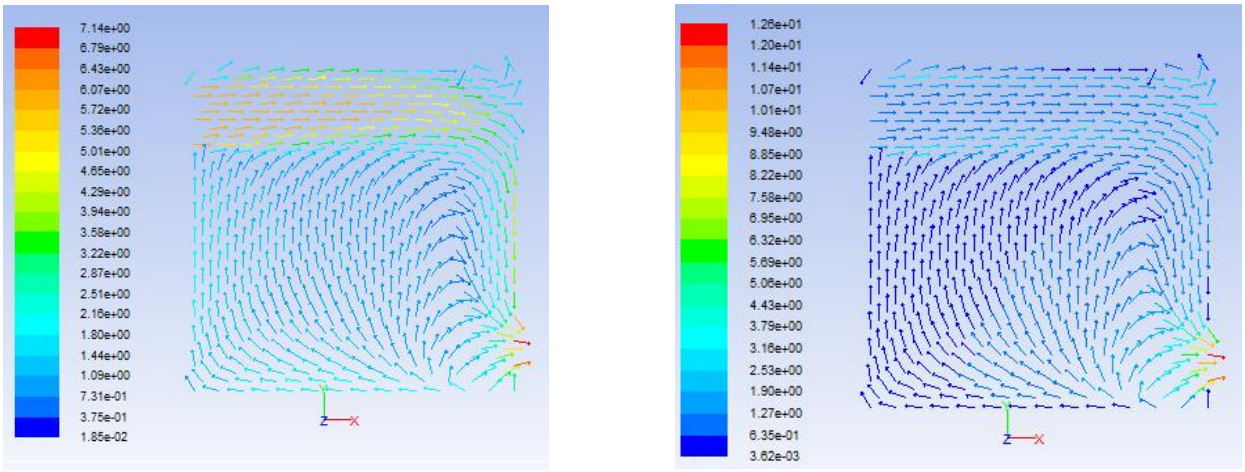

Figure E- 1: X-Velocity (left) and Turbulent Kinetic Energy (right) for w=0.6

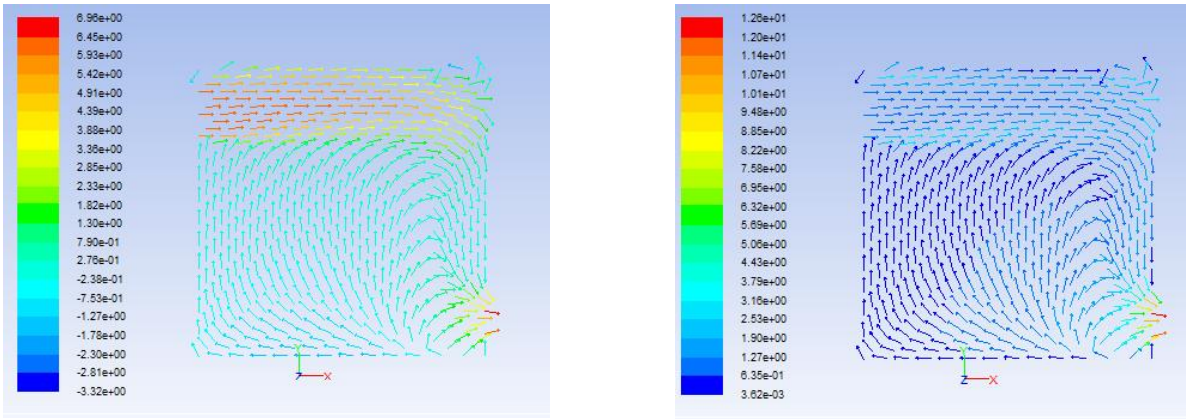

Figure E- 2: X-Velocity (left) and Turbulent Kinetic Energy (right) for w=1

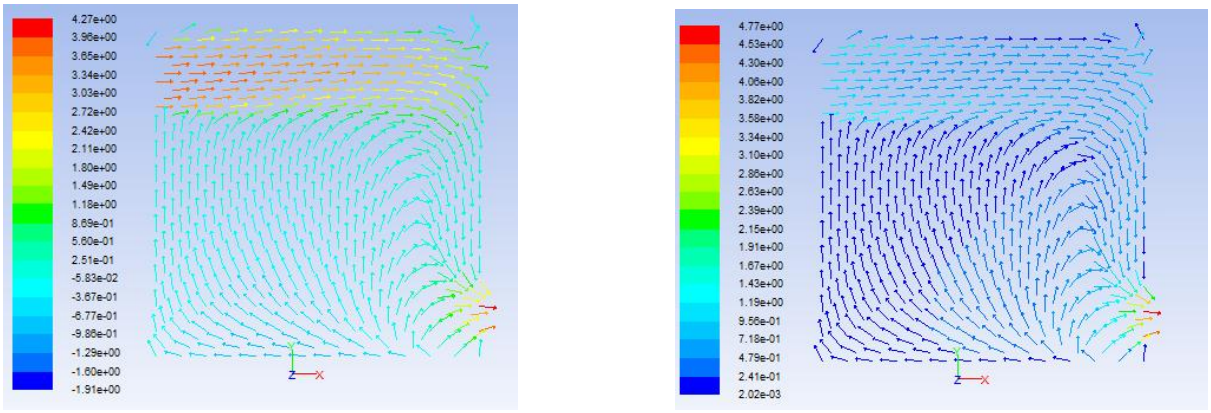

Figure E- 3: X-Velocity (left) and Turbulent Kinetic Energy (right) for γ=0.25

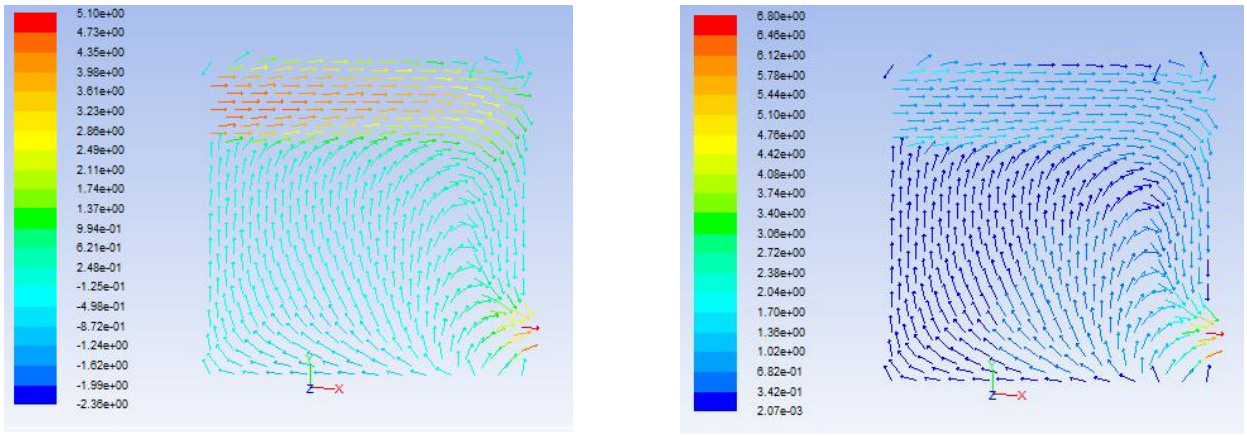

Figure E- 4: X-Velocity (left) and Turbulent Kinetic Energy (right) for γ=0.5

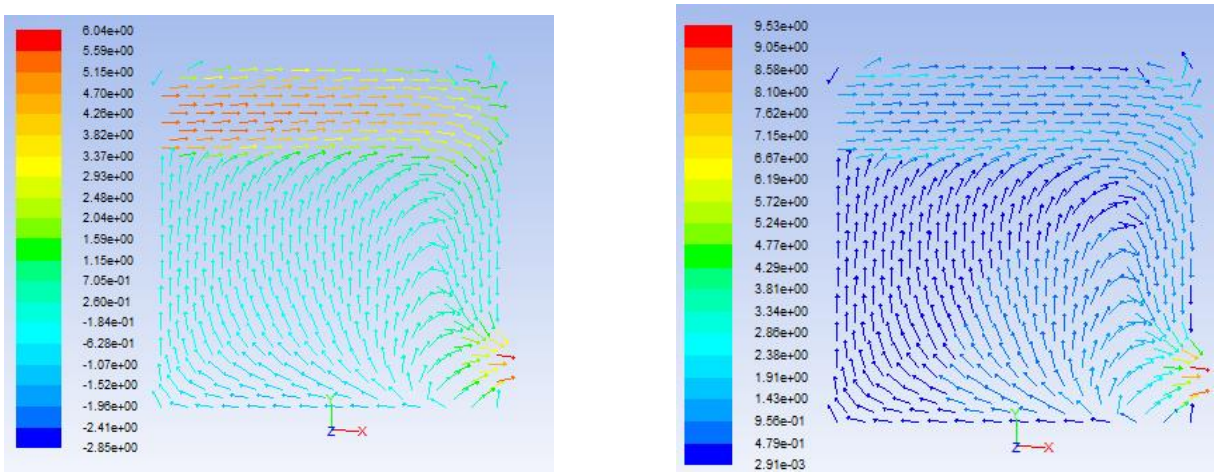

Figure E- 5: X-Velocity (left) and Turbulent Kinetic Energy (right) for γ=0.75